Review of parameterisation and a novel database (LiionDB) for continuum Li-ion battery models

O'Kane, S. E.J.; Brosa Planella, F.; Houx, J. Le; O'Regan, K.; Zyskin, M.; Edge, J.; Monroe, C. W.; Cooper, S. J.; Howey, D. A.; Kendrick, E.; Foster, J. M.; Wang, A A

[Link to publication on Research at Birmingham portal](#)

TOPICAL REVIEW • OPEN ACCESS

Review of parameterisation and a novel database (LiionDB) for continuum Li-ion battery models

To cite this article: A A Wang *et al* 2022 *Prog. Energy* **4** 032004

View the article online for updates and enhancements.

Progress in Energy

TOPICAL REVIEW

Review of parameterisation and a novel database (LiionDB) for continuum Li-ion battery models

A A Wang[1,13] , S E J O'Kane[2,13] , F Brosa Planella[3,13] , J Le Houx[4,13] , K O'Regan[5,13] , M Zyskin[6,13] ,
J Edge[7,13] , C W Monroe[8,13] , S J Cooper[9,13] , D A Howey[10,13] , E Kendrick[11,13] and J M Foster[12,13,*]

1   Department of Engineering Science, University of Oxford, Oxford OX1 3PJ, United Kingdom
2   Department of Mechanical Engineering, Imperial College London, London SW7 2AZ, United Kingdom
3   WMG, University of Warwick, Gibbet Hill Road, Coventry CV4 7AL, United Kingdom
4   Energy Technology Research Group, Faculty of Engineering and Physical Sciences, University of Southampton, United Kingdom
5   School of Metallurgy and Materials, University of Birmingham, Edgbaston, Birmingham BT15 2TT, United Kingdom
6   Department of Engineering Science, University of Oxford, Oxford OX1 3PJ, United Kingdom
7   Department of Mechanical Engineering, Imperial College London, London SW7 2AZ, United Kingdom
8   Department of Engineering Science, University of Oxford, Oxford OX1 3PJ, United Kingdom
9   Dyson School of Design Engineering, Faculty of Engineering, Imperial College London, United Kingdom
10 Department of Engineering Science, University of Oxford, Parks Road, Oxford, OX1 3PJ, United Kingdom
11 School of Metallurgy and Materials, University of Birmingham, Edgbaston, Birmingham BT15 2TT, United Kingdom
12 School of Mathematics and Physics, University of Portsmouth, Portsmouth PO1 2UP, United Kingdom
13 The Faraday Institution, Quad One, Becquerel Avenue, Harwell Campus, Didcot, OX11 0RA, United Kingdom
*   Author to whom any correspondence should be addressed.

E-mail: jamie.michael.foster@gmail.com

Abstract

The Doyle–Fuller–Newman (DFN) framework is the most popular physics-based continuum-level description of the chemical and dynamical internal processes within operating lithium-ion-battery cells. With sufficient flexibility to model a wide range of battery designs and chemistries, the framework provides an effective balance between detail, needed to capture key microscopic mechanisms, and simplicity, needed to solve the governing equations at a relatively modest computational expense. Nevertheless, implementation requires values of numerous model parameters, whose ranges of applicability, estimation, and validation pose challenges. This article provides a critical review of the methods to measure or infer parameters for use within the isothermal DFN framework, discusses their advantages or disadvantages, and clarifies limitations attached to their practical application. Accompanying this discussion we provide a searchable database, available at www.liiondb.com, which aggregates many parameters and state functions for the standard DFN model that have been reported in the literature.

1. Introduction

The growing importance of lithium-ion battery (LiB) technology motivates a search for methods to improve their design, with the aims of increasing power density, energy density, safe operating temperature range and longevity. In addition to changes in the chemistry of active materials within electrodes, design improvements require the careful optimisation of many device and system characteristics. At the cell level, optimisation might consider tab placement; cathode/anode pairing and balancing; electrode thickness, geometry, porosity, and active-material loading; separator thickness, porosity, and microstructure geometry; and quantity or composition of electrolyte [1]. At the system level, size, form factor, the number of cells and their electrical arrangement are important, as well as the overall thermal-management strategy and the methods used for performance monitoring and control.

Whilst battery design improvement can be approached purely experimentally, significant acceleration is enabled by predictive models that facilitate testing in a virtual environment, bypassing the need for slow and costly physical prototyping. Moreover, models can aid in interpreting and rationalising experimental

measurements. Various approaches to LiB modelling have been developed across a range of length scales, spanning from the atomic level up to the pack level. For example, at the atomistic scale, electronic structure calculations based on density functional theory and Monte Carlo methods are commonly used to compute intrinsic material properties, whereas packs are usually described by equivalent circuit models (ECMs). Between these two extremes is the cell level, i.e. at the scale of anode/cathode pairs; this level is the primary focus of this review. Here, models are typically physics-based and are comprised of differential equations that describe the cell as a continuum. These models are flexible with respect to empirical parameterisation. While cell components typically exhibit degrees of heterogeneity, macroscale behaviour can be represented by statistically averaged properties. These models are very-widely used, however, they are not a panacea: they require careful structuring and parameterisation specific to the device being considered. The task of the battery modeller is to consider the research questions being asked, select an appropriate model structure to address these questions parsimoniously, identify which parameters within the structure are key, and discover—via experiment, literature, or fitting—the parameter values.

The most ubiquitous cell-level battery modelling framework is the Doyle–Fuller–Newman (DFN) model, often named 'the Newman model' or the 'pseudo-two-dimensional' model. Here we shall use the DFN acronym. The DFN framework derives from porous-electrode theory, stemming from John Newman's 1961 Master's thesis under Charles Tobias [2–4], with subsequent development specific to LiBs being laid out in later foundational works [5–10]. Rigorous mathematical justification for the DFN is provided in Richardson *et al*, Ciucci and Lai, and Diaz *et al* [11–13]. The DFN framework strikes a balance between speed and complexity, incorporating detailed physics yet remaining coarse enough for efficient device-level simulations [14].

The focus of this review, namely the isothermal DFN model applied to a single anode/cathode pair, comprises a system of coupled partial differential equations (PDEs) that can contain upwards of 20 scalar parameters and around five scalar functions. Complete parameterisation is difficult, as many requisite quantities must be inferred indirectly from experimental data. Moreover, there can be significant device-to-device variability, even in cells that are ostensibly prepared in the same way. Thus, proper parameterisation is a hurdle that must be addressed to realise the maximum benefits from DFN models.

Many in the battery modelling community tend to rely on the scientific literature to find parameters, rather than carrying out their own experiments. Locating the required values in a rapidly growing body of work can be time-consuming. More importantly, great care must be taken to ensure that parameter values are extracted from raw data under assumptions that are consistent with the intended usage. The primary aim of this review is to alleviate the DFN parameterisation bottleneck in two ways. First, we survey the experimental techniques employed for parameterisation, clarifying the often unstated implicit assumptions. Elucidation of their theoretical basis empowers readers to decide what measurements can be trusted for given operating regimes. Second, we provide a searchable database (LiionDB, available at www.liiondb.com) that tabulates many parameter measurements available from the literature. The interactive database is populated by an extensive catalogue of reported parameters, as well as the details of measurement techniques used and materials characterised. Future implementations will allow the information source to continue to grow as LiB research and DFN modelling evolves.

This is not the first time that the DFN parametrisation challenge has been addressed. A recent complementary work is Laue *et al* [15], which lays out an experimental procedure for measuring parameters required for the DFN, as well as discussing the issues of identifiablility and overfitting; common pitfalls of using models with many parameters [15, 16]. Other studies, by Ecker *et al*, Zulke *et al* and Chen *et al* [17–19], carry out model parameterisation and simulation for commercially relevant cells. In all cases excellent agreement between measurement and theory is shown, demonstrating the efficacy of the DFN when proper parameterisation is provided.

This review proceeds with a brief outline of the isothermal DFN framework. Three subsequent sections focus on geometric (section 3), electrode (section 4) and electrolyte (section 5) parameters. We discuss the definition and significance of each parameter and survey reported values, providing discussion about literature consensus and any inherent variability. We then dissect the common experimental measurement approaches and critique their applicability and reliability. Finally, in section 6, we present the database (www.liiondb.com [20]), before drawing overall conclusions.

2. The DFN model

Variables and parameters involved in the standard DFN model are summarised in tables 1 and 2, respectively; the various material domains described within the framework are listed in table 3. Figure 1 illustrates the domains in a cell schematically, with porous negative-electrode (an anode during discharge), separator and positive-electrode (cathode) regions spanning positions between points $x = 0$, $x = L_n$, $x = L - L_p$ and $x = L$.

Table 1. Description of the variables used in the formulation of the full cell DFN model.

Variable	Description	Units
$c_k(x,r,t)$	Li$^+$ concentration[a] in electrode particles	mol m^{-3}
$c_{ks}(x,t)$	Li$^+$ concentration at electrode particle surface	mol m^{-3}
$c_e(x,t)$	Li$^+$ concentration in electrolyte	mol m^{-3}
$N_e(x,t)$	Molar flux of ions in electrolyte	mol m^{-2} s^{-1}
$i_k(x,t)$	Current density in electrodes	A m^{-2}
$i_e(x,t)$	Current density in electrolyte	A m^{-2}
$j_k(x,t)$	Reaction current density	A m^{-2}
$j_{k0}(x,t)$	Exchange current density	A m^{-2}
$\phi_k(x,t)$	Electrode potential	V
$\phi_e(x,t)$	Electrolyte potential	V
$T(x,t)$	Temperature	K
$\eta_k(x,t)$	Overpotential at electrode-electrolyte interface	V

[a] The electronegativity of the lithium ion is dependent upon the voltage experienced by the lithium ion. At high voltages (vs Li), it is generally ionic (Li$^+$) in nature and at low voltages vs Li it is more electronegative and likely metallic in nature (Li). Thus, it may be more appropriate to refer to this species as Li on the negative electrode side at low voltages vs lithium.

Table 2. Functions and parameters for full cell DFN model.

Param. Ftn.	Description	Value and units
F	Faraday's constant	9.6485×10^4 (A s mol^{-1})
R	Universal gas constant	8.3145 (J K^{-1} mol^{-1})
A	Planar electrode area	m^2
b_k	Particle surface area per unit volume	1 m^{-1}
c_k^{max}	Maximum Li$^+$ concentration in particle	mol m^{-3}
c_{e0}	Initial/rest Li$^+$ concentration in electrolyte	mol m^{-3}
c_{k0}	Initial Li$^+$ concentration in electrode	mol m^{-3}
D_k	Li$^+$ diffusivity in particle	m^2 s^{-1}
D_e	Li$^+$ diffusivity in electrolyte	m^2 s^{-1}
$i_{circuit}$	Applied current density	A m^{-2}
k_k	Reaction rate constant	mol m^{-2} s^{-1}
L_k	Electrode and separator thicknesses	m
L	Total cell thickness ($L_n + L_s + L_p$)	m
r_k	Particle radius	m
t_+^0	Li$^+$ transference number	—
U_k	Open-circuit potential (OCP)	V
$\mathcal{B}_k$	Liquid phase transport efficiency	—
ε_k	Electrolyte volume fraction (porosity)	—
$\varepsilon_{act,k}$	Active material volume fraction	—
σ_e	Electrolyte ionic conductivity	S m^{-1}
$\hat{\sigma}_k$	Effective solid electronic conductivity	S m^{-1}
$1 + \frac{\partial \ln f_\pm}{\partial \ln c_e}$	Thermodynamic factor	—
α_{ak}	Anodic charge transfer coefficient	—
α_{ck}	Cathodic charge transfer coefficient	—
θ_k	Electrode stoichiometry	—
Θ	Full cell state of charge	—

Table 3. Subscripts used in the formulation of the DFN model.

Subscript	Description
e	In electrolyte
n	In negative electrode/particle (anode)
s	In separator
p	In positive electrode/particle (cathode)
k	In domain $k \in \{n, s, p\}$

Figure 1. Schematic of DFN cell geometry, indicating the macroscopic and microscopic coordinate systems and domains of definition for the different variables. The positions $x = 0$, $x = L_n$, $x = L - L_p$, and $x = L$ represent domain interfaces between current collector and negative electrode, negative electrode and separator, separator and positive electrode, and positive electrode and current collector, respectively. Plotted above the particles are a snapshot of position-dependent variables during a discharge: Li$^+$ concentration c, current density i and potential distribution ϕ. The subscripts e, n and p denote the electrolyte, negative electrode and positive electrode, respectively.

In line with most other authors our DFN model is described with a single macroscopic dimension, x and a single microscopic dimension r. However, some other authors expand the macroscopic coordinates to encompass a second, or even third dimension [21, 22]. Such models are important for studying the effect of the negative electrode overhang [23] or how to improve lithiation homogeneity [24]. Strategies to systematically reduce the computational effort required to solve these macroscopically two-dimensional (2D)/three-dimensional (3D) models have also been proposed [25, 26].

A second simplifying assumption that we shall leverage throughout this review is that of isothermal conditions. Of course, in practice, temperature gradients often exist across a battery, and accounting for these exacerbates the parameterisation problem [27, 28]. Despite not giving much detail on treating temperature gradients we shall, where possible, give activation energies for material parameters where they exhibit a simple Arrhenius temperature dependence. It is worth emphasizing that restricting our interest to isothermal DFN models does not necessarily rule out using the model stated below to treat devices with thermal gradients. The reason for this is that even though pouch/roll cells may exhibit temperature variations under operation, the thermal gradients are usually not so large that neighbouring anode/cathode pairs (the part of the device described by the model below) are at significantly different temperatures. Therefore, in situations where thermal gradients are not too large, a connected network of DFN models (each at a different but uniform temperature) is a good approximation of reality. An additional thermal model is required to predict the temperature distribution across this network of DFN models but we shall not discuss this modelling aspect further. This approach has been demonstrated to be accurate in capturing thermal gradients in [25] and has been used in simulations in [21, 22, 29]. Networks of DFN models have also been used to capture mechanical stress inhomogeneities in [30, 31] as well as inhomogeneous degradation via Li-plating in [32].

Finally, we shall neglect the effects of the double-layer capacitance. This omission is well-justified when predicting the charge–discharge behaviour representative of real battery operation, but capacitive effects cannot be neglected when modelling impedance spectra where the device is stimulated on the very short timescales associated with double-layer (dis)charging [33, 34].

Both electrode materials comprise intermingled aggregates of small ($\sim 10^{-5}$ m) active particles which are connected via a sparse network of a binder with conductive solid additives and permeated by a liquid

electrolyte. The electrodes have a typical thickness on the order of 10^{-4} m and are therefore approximately one order of magnitude larger than the electrode particles. Directly finding solutions to PDEs on such a geometry is prohibitively expensive, but the DFN modelling framework circumvents this problem by posing the equations in a homogenized, multiscale fashion. The small, or microscopic, length scale is associated with individual electrode particles and the large, or macroscopic, length scale is associated with the electrode width in the direction perpendicular to the current collectors. The details and complexity of the geometry are retained in the multiscale equations (albeit in an approximate fashion) in the form of averaged parameters such as porosity and volumetric surface area that describe local geometry of phase microstructure, as well as 'effective' transport properties, whose values depend on the materials they describe, as well as the local microstructure of the multiphase medium in which the materials reside. In the remainder of this section, we outline the model and briefly discuss the physical principles that underpin each of the governing equations.

2.1. Macroscopic equations

Two main transport processes are captured on the macroscopic scale, namely (i) material balances in pore-filling liquid-electrolyte phases and (ii) electron conduction in the solid networks of active particles, binder and additives that make up the electrodes. Process (i) is captured by:

$$\frac{\partial(\varepsilon_k c_e)}{\partial t} + \frac{\partial N_e}{\partial x} = 0, \tag{1}$$

$$N_e = -\mathcal{B}_k D_e \frac{\partial c_e}{\partial x} + \left(1 - t_+^0\right)\frac{i_e}{F} + c_e v_0, \tag{2}$$

$$\frac{\partial i_e}{\partial x} = b_k j_k, \tag{3}$$

$$i_e = -\mathcal{B}_k \sigma_e \left[\frac{\partial \phi_e}{\partial x} - \frac{2RT\left(1 - t_+^0\right)}{F} \left(1 + \frac{\partial \ln f_\pm}{\partial \ln c_e}\right) \frac{1}{c_e} \frac{\partial c_e}{\partial x} \right], \tag{4}$$

in which R is the gas constant, F is the Faraday's constant, and T is the ambient temperature. Equation (1) is a material balance, which enforces continuity of the anion concentration, c_e—this equals both the salt concentration and cation concentration as a consequence of the local electroneutrality approximation. (It will always be assumed here that the anion of the lithium salt dissolved in the electrolyte is monovalent.) Equation (2) is a constitutive law for the total molar flux of anions N_e, which accounts for contributions due to diffusion, driven by concentration gradients, migration, driven by the ionic current density i_e, and convection, driven by the solvent velocity v_0. Typically, convection is neglected, so v_0 vanishes. The migration term accounts for excess flux arising from differences in the relative mobilities of cations and anions. By convention this effect is typically parameterized in terms of a cation transference number relative to the solvent velocity, t_+^0, which measures the fraction of electrolyte conductivity contributed by cation mobility; the anion transference number $\left(1 - t_+^0\right)$ appears in the flux law here. Diffusion is parametrized by the salt diffusivity in free liquid, D_e.

In (1) and (2), coefficients taking a subscript k transform the material properties of the free liquid electrolyte into effective values attained when the electrolyte permeates a pore structure within domain k. Thus, the volume fraction of phase k occupied by electrolyte, ε_k, appears in the material balance, to make c_e represent the anion concentration that would be recorded if electrolyte was extracted from the pores within phase k and measured separately. Similarly, the transport efficiency $\mathcal{B}_k$ appears in the flux law, to account for how pore shapes and connectivity lower the apparent salt diffusivity from D_e, its value in free liquid. Generally, pore networks with lower porosity and greater tortuosity cause $\mathcal{B}_k$ to reduce from its maximum value of 1. Note that no geometric correction is needed for transference numbers; since they inherently describe a ratio of mobilities, corrections for pore geometry cancel out.

Equation (3) is a charge balance in the electrolyte phase, whose form derives from considering the material balances of cations and anions together, under the local electroneutrality approximation, and an assumption that ion fluxes entirely determine the current density through Faraday's law. A source term appears, dependent on the electrode–electrolyte interfacial current density j_k, which describes the rates at which electrochemical reactions occur on pore surfaces. In porous electrodes, j_k quantifies the kinetics of intercalation or deintercalation reactions. Since effective reaction rates also depend on the pore surface area contacted by electrolyte, the generation term in the charge balance scales with a second geometric parameter b_k, which describes the electrochemically active surface area per unit volume of the pore network in domain

k. In the DFN it is assumed that the electrode particles are spherical and equally-sized, from which it follows that b_k is related to the effective particle radius r_k and the particle volume fraction $\varepsilon_{\mathrm{act},k}$ via

$$b_k = 4\,\pi r_k^2 \left(\frac{\varepsilon_{\mathrm{act},k}}{\frac{4}{3}\pi r_k^3} \right), \tag{5}$$

where the right-hand side of this equation can be seen to be a product of the surface area of a single particle $(4\,\pi r_k^2)$ and the number density of electrode particles. The latter is the quantity inside the parenthesis, and this is in turn the ratio of the volume fraction (or volume density) to the volume of a single electrode particle. Kirk *et al* [35] have considered how to generalise the DFN model to include heterogeneity in particle sizes across the electrode thickness.

It is worth emphasizing that we shall generally adopt the convention of denoting bulk current densities with i_k and interfacial current densities with j_k. Observe that by convention, the current j_k is taken to be positive when a reaction is driven anodically, i.e. when positive charges enter the liquid from the solid phase.

Equation (4) is the MacInnes equation, a modified form of Ohm's law. As well as relating the ionic current density to the gradient of potential ϕ_e in the electrolyte through its ionic conductivity σ_e, the MacInnes equation also includes a correction to account for concentration overpotential—the potential drop associated with differences in the free energy of mixing that accompany concentration polarization. This term injects another material parameter, the thermodynamic factor $1 + \partial \ln f_\pm / \partial \ln c_e$, which accounts for possible deviations from ideal Nernstian behaviour.

Note that the DFN model may also be stated in an equivalent form that includes an explicit balance of the Li^+ cations. This can replace either the anion balance or the charge balance, as it depends linearly on those two relationships. The form adopted here is computationally most convenient because LiB electrodes are typically anion blocking. Thus the anion balance equation involves no source terms, a simplification which can be advantageous for numerical solutions, either with finite differencing or the finite-element method.

Electron conduction in the anode and cathode is captured by:

$$\frac{\partial (i_k + i_e)}{\partial x} = 0, \tag{6}$$

$$i_k = -\hat{\sigma}_k \frac{\partial \phi_k}{\partial x}. \tag{7}$$

Here, i_k is the current density in the solid phase within domain k, ϕ_k is the potential there, and $\hat{\sigma}_k$ is its effective electronic conductivity. As in the electrolyte-phase governing system, the former equation (6) ensures charge conservation, whereas (7) is a constitutive relation, stating that electron conduction is ohmic. The first equation here expresses overall charge continuity across a volume element of domain k. Note that this balance equation could be restricted to the solid phase, including a generation term analogous to the one in the charge balance of (3), but it is easier to handle the total current density $i_k + i_e$ analytically because it is solenoidal (divergence-free) as a consequence of electroneutrality. Observe that $\hat{\sigma}_k$ could in principle be deconvolved into contributions from the different electron-conducting phases that make up the electrode and a geometric factor, analogous to $\mathcal{B}_k$, could be included explicitly, but it is not conventional. We believe that this is likely because it is relatively straight-forward to measure $\hat{\sigma}_k$ directly by experiment.

The local interfacial current density j_k is typically determined by reaction kinetics in electrode domains, and taken to vanish in the separator. Thus

$$j_k(x) = \begin{cases} j_{\mathrm{n}} & \text{if} \quad 0 \leqslant x \leqslant L_{\mathrm{n}}, \\ 0 & \text{if} \quad L_{\mathrm{n}} < x \leqslant L - L_{\mathrm{p}}, \\ j_{\mathrm{p}} & \text{if} \quad L_{\mathrm{p}} < x \leqslant L, \end{cases} \tag{8}$$

with kinetic rate laws for the nontrivial terms determined by considering reaction mechanisms.

2.2. Macroscopic boundary and interface conditions

At the extremities of the cell where the electrodes meet the current collectors, there is no flux of anions and no ionic current; the current in the solid network equals that provided or extracted by the external circuit. At the internal interfaces, where the anode and cathode meet the separator, the current density in the solid network must be zero, because the separator is electronically insulating. As such, the macroscopic equations are supplemented by boundary conditions

$$i_{\mathrm{n}}|_{x=0} = i_{\mathrm{circuit}}(t), \tag{9}$$

$$N_e|_{x=0} = 0, \tag{10}$$

$$i_e|_{x=0} = 0, \tag{11}$$

$$i_n|_{x=L_n} = 0, \tag{12}$$

$$i_p|_{x=L-L_p} = 0, \tag{13}$$

$$i_p|_{x=L} = i_{circuit}(t), \tag{14}$$

$$N_e|_{x=L} = 0, \tag{15}$$

$$i_e|_{x=L} = 0, \tag{16}$$

where $i_{circuit}(t)$ is the current density provided by the battery to the circuit. We use the convention that positive charge moving rightwards constitutes a positive current; as such positive values of $i_{circuit}(t)$ correspond to discharge and negative ones to charge. In situations where the current is known, $i_{circuit}(t)$ can is specified. However, in many situations either the voltage, or power is known and in these cases an additional equation in required in order to solve for the as yet unknown current $i_{circuit}(t)$.

2.3. Microscopic equations and boundary conditions

The Butler–Volmer laws (introduced below in (20)) determine the interfacial current density j_k which in turn depends strongly on the concentration of intercalated Li$^+$ at the surfaces of active particles in the solid phase, c_{ks}. Determination of c_{ks} necessitates the solution of an appropriate transport or reaction model describing the dynamical distribution of Li within the particles, at every location within the macroscopic dimension, x. Transport within particles occurs on a smaller, microscopic scale, taken to be a pseudo-second dimension r orthogonal to x. We take r to be the radial position within a spherical particle and let r_k be the radius of a particle in domain k.

Under the assumption that intercalated lithium sits in a solid solution, a diffusion model for transport in the active particles is appropriate. For simplicity we outline a nonlinear spherical diffusion equation for use in the particle dimension, noting that multiple studies have demonstrated its wide efficacy for fitting experimental trends [36–39]. In this case the microscopic equations and boundary conditions are:

$$\frac{\partial c_k}{\partial t} = \frac{1}{r^2}\frac{\partial}{\partial r}\left(r^2 D_k \frac{\partial c_k}{\partial r} \right), \qquad\qquad \text{in } 0 < r < r_k, \tag{17}$$

$$\frac{\partial c_k}{\partial r} = 0, \qquad\qquad \text{at } r = 0, \tag{18}$$

$$-D_k \frac{\partial c_k}{\partial r} = \frac{j_k}{F}, \qquad\qquad \text{at } r = r_k, \tag{19}$$

where D_k represents the Li-ion solid-state diffusivities in electrode k, generally dependent on composition and temperature. Equation (17) is a material balance for intercalated lithium and (18) is the condition of boundedness of the concentration, ensuring that concentration remains finite at the particle core. Boundary condition (19) ensures through kinetic model (20) and (21) that the Li$^+$ flux leaving the electrolyte balances that entering the particles. We should emphasise the assumption that electrode particles are spherical here. This is often far from being true, but it is unclear that accounting for more complex particle-scale geometries in fact leads to observably different outcomes. More complex geometries have been considered [40–42], but this often entails solving microscopic transport equations in a higher number of spatial dimensions, which is more computationally intensive and undermines the efficiency of the framework.

There is considerable debate about what equations are most appropriate to describe interfacial reactions and solid-state lithium transport within intercalation particles. In the original papers by Newman and coworkers [5, 6, 8], a spherical form of Fick's second law of diffusion was adopted, but other models, including shrinking-core [14, 43, 44] and Cahn-Hilliard [45], have been proposed subsequently to handle

Table 4. Experimental techniques and individual cell component parameters that they measure. Techniques marked with a dagger (†) can be applied to cells which are received already constructed (i.e. in a full cell configuration), but in order to isolate the components of a single electrode, cells are often torn down and reassembled as part of half cell. Techniques that are not marked with a dagger necessarily require teardown.

Technique	Model parameter(s) extracted	Sections for discussion
Microscopy	$L_k, r_k, \varepsilon_k, \varepsilon_{\text{act},k}, \mathcal{B}_k$	§ 3.2.1
EIS †	$\mathcal{B}_k, k_k, D_k, D_e, \sigma_e, t_+^0$	§ 3.2.2, § 4.2.6, § 5.2.1
XRD	r_k	§ 3.2.3
Hg porosimetry	$\varepsilon_k, \varepsilon_{\text{act},k}, b_k$	§ 3.2.4
BET adsorption	b_k	§ 3.2.5
Electronic conductivity probe	$\hat{\sigma}_k$	§ 4.2.1
pseudo-OCV †	U_k	§ 4.2.2
GITT †	$U_k, D_k,$	§ 4.2.3
SC GITT †	$k_k,$	§ 4.2.3
CV †	k_k, D_k	§ 4.2.4
PITT †	k_k, D_k	§ 4.2.5
Polarisation-relaxation cells	D_e, t_+^0	§ 5.2.2
Concentration cells	$1 + \dfrac{\partial \ln f_{\pm}}{\partial \ln c_e}, t_+^0$	§ 5.2.3
Densitometry	$\overline{V}_e, \overline{V}_0$	§ 5.2.5

materials where phase-transformation reactions [46, 47], rather than diffusion dynamics, govern the distribution of intercalated lithium. Such materials may also require alternative forms of the microscopic kinetic rate laws.

In an elementary intercalation process, lithium ions are assumed to enter or leave the liquid to occupy available sites in the crystal lattice of an intercalation compound, in which intercalated lithium atoms form a solid solution. Interfacial current is governed by a system of kinetic rate laws of the form

$$j_k = j_{k0} \left[\exp \left(\frac{F \alpha_{\text{ak}}}{RT} \eta_k \right) - \exp \left(-\frac{F \alpha_{\text{ck}}}{RT} \eta_k \right) \right], \tag{20}$$

$$j_{k0} = F k_k \left(\frac{c_e}{c_{e0}} \right)^{\alpha_{\text{ck}}} \left(\frac{c_{ks}}{c_k^{\max}} \right)^{\alpha_{\text{ak}}} \left(1 - \frac{c_{ks}}{c_k^{\max}} \right)^{\alpha_{\text{ck}}}, \tag{21}$$

$$\eta_k = \phi_k - \phi_e - U_k(c_{ks}). \tag{22}$$

Here, j_{k0} is termed the exchange current density, c_{ks} is a variable representing the concentration of intercalated lithium at the active-particle surface, and the surface overpotential η_k expresses the difference between the liquid–solid potential drop and the equilibrium potential U_k, the latter being a state function dependent on c_{ks}. The kinetic model involves various parameters as well: k_k is the rate constant for the intercalation half-reaction, c_{e0} is the reference concentration of anions in the electrolyte at which k_k is measured, $c_k^{\max}$ is the maximum concentration of lithium that can be intercalated into the electrode material, and α_{ak} and α_{ck} represent the charge-transfer coefficients for the anodic and cathodic directions of the half-reaction in electrode k, respectively. Note that k_k is alternatively known as the reaction rate or exchange coefficient, depending on the model used [19, 48].

2.4. Initial conditions
Initial conditions are required for the ionic concentration in the electrolyte, as well as the Li concentration in the negative and positive electrode particles. Assuming an initially equilibrated state at rest, one can set

$$c_n|_{t=0} = c_{n0}, \tag{23}$$

$$c_p|_{t=0} = c_{p0}, \tag{24}$$

$$c_e|_{t=0} = c_{e0}, \tag{25}$$

where c_{k0} is the initial concentration in electrode k and c_{e0} is that in the electrolyte. Section 4.1.1 discusses the challenges in determining appropriate values for c_{k0}, often inferred from the cell voltage, and how individual electrode lithiation is linked to the overall cell state of charge.

2.5. Full cell potential

Computed solutions of the full-cell DFN model can be used to compute potentials at the negative and positive current collectors, V_n and V_p respectively, via the relations

$$V_n(t) = \phi_n\big|_{x=0}, \tag{26}$$

$$V_p(t) = \phi_p\big|_{x=L}. \tag{27}$$

Hence the terminal voltage V measured for a full cell is

$$V(t) = V_p(t) - V_n(t). \tag{28}$$

This is the cell voltage that should be used to make comparisons between the model and experimental data. It is often helpful to bear in mind that the cell potential, V, is composed of several parts, namely: (i) the potential drop across the solid parts of each electrode (associated with electron conduction), (ii) the OCVs between each electrode and the electrolyte, (iii) the reaction overpotentials between each electrode and the electrolyte and (iv) the potential drop across the electrolyte (associated with ionic conduction) [49]. An appealing way to visualise these different contributions is via a transmission-line model [50], in which there are two parallel branches, each containing resistors, representing the conduction in the solid and electrolyte, respectively. These two branches are connected by a number of nonlinear elements in parallel with one another, representing the (de)intercalation reactions that transfer charge between the electrolyte and solid. A sketch of this transmission line interpretation is given in Castle *et al* [51].
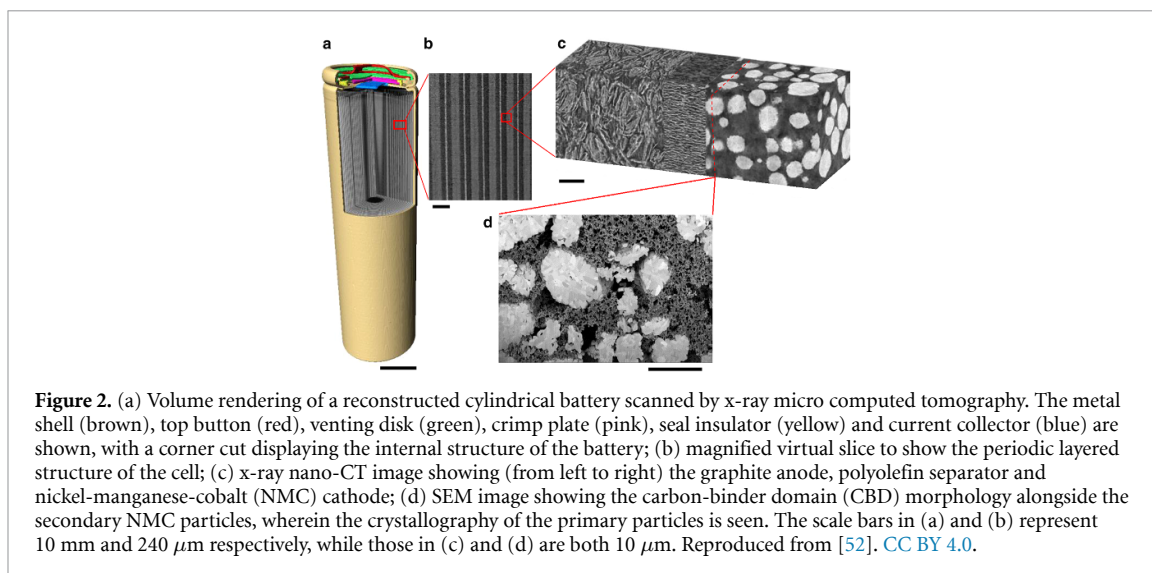
3. Geometrical parameters

The geometric configuration and the domain morphologies of the cell, are determined by manufacturing processes, as well as the inherent structures of their constituents. The choice and balance of components in a given domain determines properties such as active surface area and porosity, and, in turn, these factors significantly influence cell performance. To minimise repetition in the following subsections, it should be stated that although volume fractions, particle sizes, surface areas and tortuosity factors are all typically reported as single, averaged values within each domain (i.e. anode, separator and cathode), they can all vary as functions of position within any domain as well. Component dimensions may also be influenced by the process of cell assembly or teardown, e.g. a separator's thickness is larger when unconfined than under the mechanical loading present inside an assembled battery. Renderings of the different layered components are illustrated in figure 2. Although the various geometrical parameters are discussed in turn, they are intimately linked and in practice it is often not possible to vary them independently. For example, altering average particle radius also alters the surface-to-volume ratio available for electron exchange and effective transport factors.

3.1. Parameters

3.1.1. Layer thickness

The layer thicknesses of components within the cell, as depicted in figure 1, are straightforward to understand and relatively easy to measure, e.g. using calipers or a micrometre gauge. Electrode layer thicknesses are closely linked to the areal capacities of active material coatings. Reported electrode thicknesses either measured or used in DFN models typically fall in the 10–100 μm range, and commercial polymer separator thicknesses in the 15–30 μm range. Layer thicknesses may be affected by the fabrication process, so these properties should be understood as their values after cell formation. This distinction is particularly important for the separator, which is usually made of a porous polymer, whose thickness prior to cell construction can be substantially different from the thickness after being wetted with electrolyte and wound or stacked in a cell, incurring a static mechanical load.

It is also possible that layer thicknesses can change with cycling of a battery, a process that requires further characterization and modelling. These temporal variations are almost always neglected in DFN models, where thicknesses for the electrodes and separator are usually taken to be those measured individually, prior to assembly [17], or following teardown after use [19]. Volume expansion or contraction of the active materials accompanies the lithiation/delithiation processes [53, 54], which is causes concomitant thickening/thinning of the electrodes. For silicon-based anodes, the volume expansion associated with lithiation is so large (up to ~400% for pure Si) that it cannot be justifiably neglected. In that

Figure 2. (a) Volume rendering of a reconstructed cylindrical battery scanned by x-ray micro computed tomography. The metal shell (brown), top button (red), venting disk (green), crimp plate (pink), seal insulator (yellow) and current collector (blue) are shown, with a corner cut displaying the internal structure of the battery; (b) magnified virtual slice to show the periodic layered structure of the cell; (c) x-ray nano-CT image showing (from left to right) the graphite anode, polyolefin separator and nickel-manganese-cobalt (NMC) cathode; (d) SEM image showing the carbon-binder domain (CBD) morphology alongside the secondary NMC particles, wherein the crystallography of the primary particles is seen. The scale bars in (a) and (b) represent 10 mm and 240 μm respectively, while those in (c) and (d) are both 10 μm. Reproduced from [52]. CC BY 4.0.

case some modelling work has aimed to extend the DFN framework to couple volumetric changes with cell electrochemistry, see for example McDowell *et al* [55] and Zhang *et al* [56].

3.1.2. Volume fractions
The two electrodes usually contain four distinct phases: active-material particles, a conductive additive, a polymeric binder, and the pore-filling phase. The conductive additive, most commonly carbon black, is present to increase the electronic conductivity of the composite electrode, aiding electron transfer between the particles and current collector. It is often extremely fine (much finer than the electrode particles) and is typically well mixed with polymeric binder, such that the two phases are hard to distinguish using most imaging techniques. For the purposes of DFN modelling these two phases are usually lumped together and referred to collectively as the carbon–binder domain (CBD). Note that incomplete wetting by electrolyte during cell formation or side reactions during cycling can lead to the formation of a fifth, gaseous pore-filling phase [57], which is typically neglected in DFN models for Li-ion cells, although it has been considered in some cases [58].

Many models, including the original DFN models, set the volume occupied by the CBD to zero [5, 6, 19]. This assumes that cells are manufactured to maximise energy density by minimising the required CBD volume. As such, the electrolyte and active material volume fractions are related via:

$$\varepsilon_k + \varepsilon_{\text{act},k} = 1. \tag{29}$$

Here, ε_k is the electrolyte volume fraction (or solid-phase porosity) and $\varepsilon_{\text{act},k}$ is the active-material volume fraction. Figure 3 illustrates the distribution of porosities for positive and negative electrode materials, along with polymer separators sampled from the LiionDB parameter database. Porous electrodes in LiBs have electrolyte volume fractions of approximately 0.4–0.5, while separators skew towards higher porosities.

Neglecting the CBD volume fraction via the assumption of spherically symmetric electrode particles ignores the fact that parts of an electrode particle's surface will be in contact with the CBD, instead of the electrolyte, resulting in some portion of the particle's surface not being available for (de)intercalation. This sort of consideration could dramatically impact model assumptions, particularly the spherically symmetric diffusion approximation in the microscopic equations and boundary conditions.

The only role that the CBD plays in the model equations presented here is indirect: the CBD volume fraction determines the effective electronic conductivity of the electrodes, $\hat{\sigma}_k$, a quantity that is typically measured directly using electrochemical impedance spectroscopy (EIS). The active-material volume fractions, in combination with the layer thicknesses, are needed to determine the theoretical areal capacity of the cell. They are also used to calculate the maximum Li concentration in active materials, as well as for anode–cathode stoichiometric balancing, as discussed in section 4.1.2. The electrolyte volume fraction has a significant role in determining the rate performance of the cell, because it impacts the transport of ions in the electrolyte required for charge transfer. Further discussion of porosity and its effect on transport efficiency is provided in section 3.1.5. On a practical note, incomplete electrolyte infiltration within pores is known to reduce cell performance. Gas generation from degradation during operation may also cause additional inactive regions [57, 59].
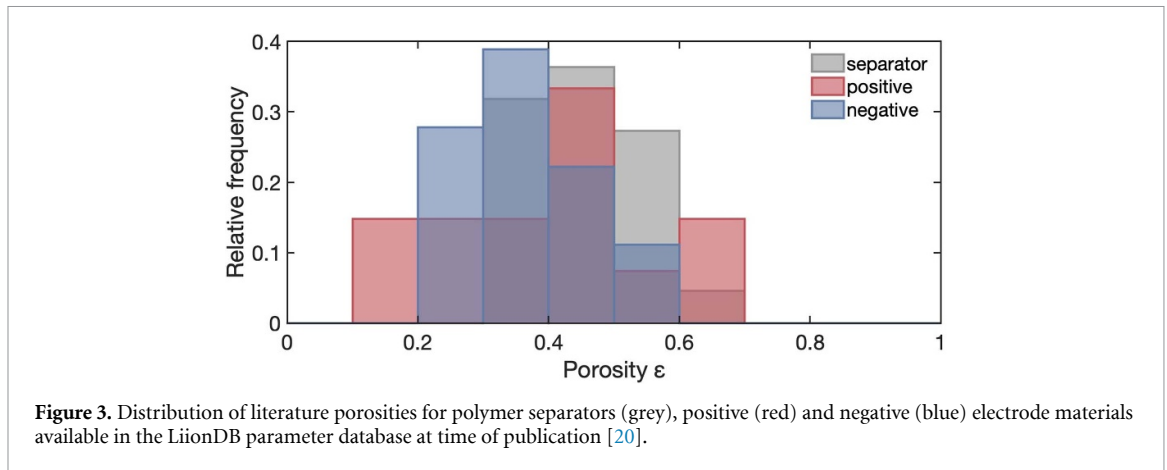
Figure 3. Distribution of literature porosities for polymer separators (grey), positive (red) and negative (blue) electrode materials available in the LiionDB parameter database at time of publication [20].
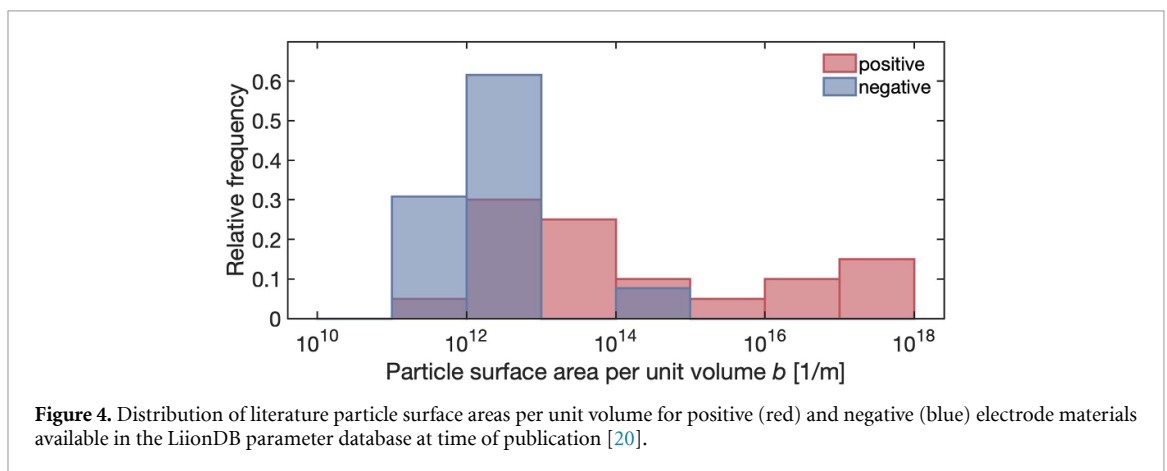

Figure 4. Distribution of literature particle surface areas per unit volume for positive (red) and negative (blue) electrode materials available in the LiionDB parameter database at time of publication [20].

3.1.3. Particle surface area per unit volume
The surface area of active material that is available for intercalation per unit volume of electrode, b_k, depends on the size and shape of the active particles as well as their arrangement with respect to the CBD [35]. It comes into the liquid-phase charge balance in (3) when relating the local interfacial current densities on pore surfaces to the current transferred per unit of porous-electrode volume. As such, the surface-area to volume ratio impacts the rate at which lithium can transfer between the liquid electrolyte and the solid active materials.

Naively, one might expect that b_k should be maximised for the optimal performance (to provide lots of surface area for intercalation); however, in reality, the active material surfaces tend to form a layer called the solid electrolyte interphase (SEI), which consumes lithium inventory, thereby decreasing device capacity, and so a balance must be struck. In addition, the practicalities of manufacturing with very fine powders, which are hard to produce and process, can also be a consideration.

As highlighted in section 3.2, and plotted in figure 4, the measured surface area varies dramatically depending on the measurement technique used. There is also little consensus on the choice of surface area, with literature measurements choosing between definitions such as: (a) the whole solid-pore interface (i.e. including CBD surface), (b) the active particle surface area, and (c) the active particle-pore interface. As stated in section 4.1.3, the surface area defined must be paired carefully with measured exchange current densities to parameterise electrode kinetics consistently.

3.1.4. Radius of electrode active particles
The radii of the active-material particles establish the distance that intercalated lithium need to diffuse to reach the core, as well as determining the characteristic relaxation time of solid-phase diffusion, which in turn controls rate performance. Large particles do not perform well at high rates, because the depletion of or saturation with lithium at particle surfaces limits the accessible range of reaction current, thereby inhibiting performance by lowering power efficiency.

Real electrodes contain a distribution of particle sizes and shapes that confounds the determination of a single representative radius for each electrode, as is required by the basic DFN model [60]. For
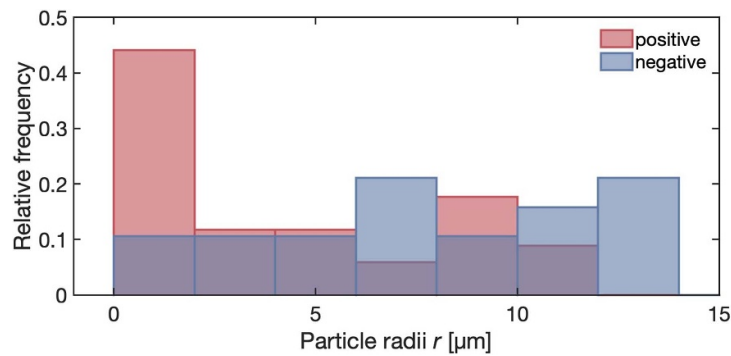
Figure 5. Distribution of literature radii for positive (red) and negative (blue) electrode particles available in the LiionDB parameter database at time of publication [20].
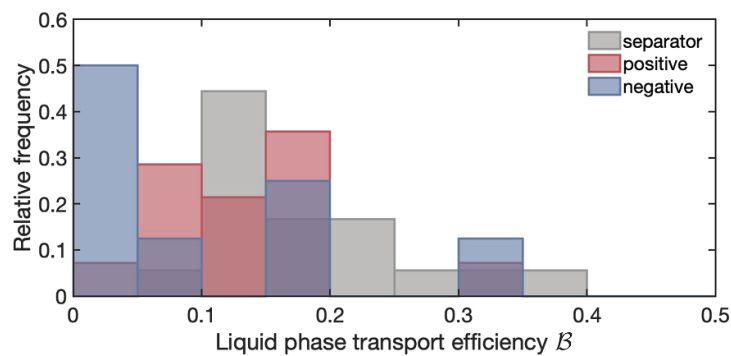

Figure 6. Distribution of liquid-phase transport efficiencies in polymer separators (grey), and positive (red) and negative (blue) electrodes available in the LiionDB parameter database at time of publication [20].

polycrystalline materials, the choice of a characteristic length based on primary or secondary agglomerated structures can change the radius parameter by a factor of 20 [61]. Particle radii tend to fall below 20 μm according to figure 5. The spread in the literature owes to the choice of primary or secondary structures, along with the variation among active materials.

The particle radius plays a large role in the way intrinsic parameters of an electrode material are extracted, as discussed in section 4. While average radii are adequate for most models, newly engineered electrodes with graded radii may require models that treat particle radii as a variable with position [35, 62]. Different approaches towards averaging can also alter the effective radii [35]. In addition, some materials, such as graphite platelets, tend to form highly non-spherical particles [40, 63]. Anisotropic lithium diffusivities also result in different observed behaviours than that expected for an isotropic sphere (particularly in the case of graphite) [64]. For these reasons, defining a particle radius to characterise and model electrode geometries is not straightforward, even if all of the true morphological information is known.

3.1.5. Effective transport properties for electrolytes in pore networks

The original DFN formulation captures the impact of pore-network geometry on electrolyte transport properties by using effective transport parameters $D_{\text{eff},k}$ and $\sigma_{\text{eff},k}$. When a diffusion medium can be suitably homogenized, the domain-specific properties of a pore-filling electrolyte relate to their values in an unobstructed electrolyte through a domain-specific transport efficiency, $\mathcal{B}_k$, as mentioned above. Figure 6 shows that transport through the porous layers in LiBs is typically constricted by more than 60%.

It is also common to see MacMullin numbers ($N_{\text{M},k}$) being used to quantify the hindrance of transport caused by the electrode geometry [65]. As $\mathcal{B}_k$—the inverse of $N_{\text{M},k}$—is bounded between 0 and 1, it is comparatively more convenient for manipulation and interpretation. Transport efficiency is often further decomposed into two distinct contributions: the reduction due to the pore volume fraction, captured by ε_k, and the reduction due to the pore tortuosity factor, τ_k. The four macroscopic factors that characterize pore networks relate through

$$\mathcal{B}_k = \frac{1}{N_{\text{M},k}} = \frac{\varepsilon_k}{\tau_k}. \tag{30}$$

Measurement and interpretation of tortuosity factors has been the subject of extensive discussion [66].

Fuller *et al* [6] make use of the well-established Bruggeman correlation (i.e. $\tau_k = \varepsilon_k^{1-b}$, where *b* is 1.5 for effective transport through spherical packed beds) to approximate the tortuosity factor. We note that there are some subtleties in how Doyle *et al* [5] implement the correction; for example, they take a factor of ε_k out from $D_{\text{eff},k}$, since their variable N_e describes anion flux through a whole volume element, whereas their c_e is the concentration of anions in the pores.

Bruggeman's tortuosity correlation is commonly deployed in situations where experimental geometrical information is limited. Although it is a convenient means to approximate the effect of microstructure on transport, it has been shown that the assumptions in its derivation do not necessarily align with the conditions established by the microstructures of real battery electrodes [67]. For example, use of a Bruggeman factor suggests that all electrodes with the same average particle radii and porosity would have the same pore-phase transport properties, but this is clearly not the case. Although correlations can be extended to account for more complex scenarios [68], many additional simplifications and assumptions are still required.

Unlike porosity, which has a meaningful definition within a planar differential cross section (ratio of cut-through pore area to total plane area), the tortuosity factor (and therefore $\mathcal{B}_k$ and $N_{\text{M},k}$) does not. This is because the tortuosity factor is an emergent property of transport through a microstructure; therefore sufficient path length (i.e. representative volume) is required before a value can be meaningfully measured. The multiscale approach used to construct the DFN model assumes that the characteristic lengthscale of the electrode particles is negligible compared to that of the electrode thickness, but this is not the case, with typical scale differences of only a single order of magnitude. The error that this incurs is likely to be related to the ratio of particle size to electrode thickness, i.e. of the order of 10%.

More recently, alternative concepts, including the 'electrode tortuosity factor' [69] have been reported that are able to measure the effect of graded microstructures. Many literature examples report 'geometrical tortuosities' or 'path-length tortuosities', calculated using a wide variety of algorithms applied to image data. This is distinct from the tortuosity factor which is found from using the multiscale approach. However, as made clear by Epstein [70], although path-length tortuosities are relevant to systems with well-defined paths, e.g. rivers and veins, they are not relevant to the types of microstructure found in real battery electrodes, unless they happen to consist of 'capillary' pores with relatively constant cross section.

3.1.6. Effective electrode solid conductivity

In DFN models, the effective electronic conductivity of the electrodes is often assumed to be constant within each electrode, taking values of $\hat{\sigma}_n$ and $\hat{\sigma}_p$) in the negative and positive sides respectively. Probe methods capture the effective conductivities directly, and are therefore usually adopted in practice, although two-electrode measurements of direct-current resistance are sometimes used [71, 72]. Although the active particles are electronically conductive, they have a much lower conductivity than the CBD, and so it is often relatively accurate to approximate the conductivity of the electrode as a whole using only a contribution from the porous CBD. In practice, electronically-isolated regions of active material can become disconnected from the CBD network [73]. In reality such particles are then inert, and cannot participate in battery operation, but these local effects are not captured by the effective quantities.

3.2. Measurement/fitting techniques

3.2.1. Imaging

Scanning electron microscopy (SEM) and transmission electron microscopy (TEM) have been used extensively for 2D image acquisition. SEM scans a beam of electrons across the target in a raster pattern and then detects the scattered electrons, with some devices achieving a resolution of below 1 nm [74]. By contrast, TEM transmits electrons through the sample before being detected, offering a way of capturing the internal detail, such as crystal structure and morphology. Additionally, TEM can achieve finer resolution than SEM, with some reports of 50 pm. However, samples need to be less than $\sim 10^{-7}$ m thick (much thinner than practical electrode coatings) to allow full electron penetration.

2D images can then be processed to extract measurements for layer thicknesses, particle radii and particle size distributions. It is important to note that because sample sizes are often very small compared to the entire electrode, a given image may not be statistically representative of the whole structure. It is generally difficult to obtain sufficiently large datasets that are truly representative for analysis.

Both focused ion beam-scanning electron microscopy (FIB-SEM) and x-ray computed tomography (XCT) have been used extensively in 3D studies; many examples can be found in fuel cell [75, 76], and battery research [77–79]. The FIB-SEM method images the 2D surface using an SEM, with the same resolution capability as SEM, and then mills the surface away using a controlled beam of charged positive particles, typically gallium, to reveal another layer. These 2D images are then reconstructed to produce a 3D

microstructural volume. The milling process means FIB-SEM is destructive, i.e. *in situ* or *operando* imaging is not possible [80]. XCT systems fire an x-ray source at the sample and measure the resulting attenuation pattern, producing a 2D projection image. The sample is rotated to obtain images from many angles, which are then reconstructed, typically through a back-projection algorithm, to produce a 3D volume [81]. Image analysis methods are used to directly characterise the 3D microstructure, helping to understand particle distribution and anisotropy [82–84].

Image-based simulations can calculate geometric parameters, such as effective conductivities and volume fraction. Several open-source tools and methods for data processing are available [85]. Two popular options are (i) TauFactor, an open-source MATLAB (MathWorks) application for efficiently calculating the tortuosity factor, volume fraction, surface area and triple phase boundary density from image-based microstructural data [86] and (ii) OpenPNM, an open-source software package developed in Python for performing physics-based pore network simulations [87]. Other image-based mesostructure simulations also account for the CBD in electrode models, to elucidate effective transport properties and extensions into mechanical stresses [88, 89].

3.2.2. Electrochemical impedance spectroscopy

EIS is an electrical technique useful to probe various phenomena within LiBs [90]. This section describes the technique but focuses on geometric parameters; sections 4.2.6 and 5.2.1 will address material and interfacial properties.

The EIS method consists of applying a small sinusoidal voltage or current perturbation and recording the respective current or voltage response, whose resulting amplitude and phase shift quantify the impedance; an impedance spectrum is then recorded as a function of the frequency of the excitation signal. Although frequencies ranging from μHz to MHz are in principle accessible, most information is gathered in the range between 0.1 Hz and 100 kHz, where signal-to-noise ratios are good and reproducibility is easier to achieve. EIS provides multiscale resolution, because different physicochemical processes have distinct characteristic timescales, excited at different frequencies within the sampled spectrum.

Diffusive transport—both in electrode active particles and the electrolyte—has characteristic frequencies in the range below 1 Hz. Interfacial effects, such as charge-transfer resistance (kinetic rate constants), double-layer capacitance, and possibly effects arising from surface passivation are resolved at intermediate frequencies, between 1 Hz and 1 kHz. At higher frequencies, above 1 kHz), ohmic and ionic resistance and inductance can be observed. Notably, the linkage between impedance data and material or geometric parameters requires an appropriate model be fitted to the observed spectrum. Often the choice is an ECM whose parameters relate heuristically to physical parameters [91, 92], but formally linearised electrochemical models may also be used [16, 93].

Generally, division of the effective electrolyte conductivity extracted from EIS by the ionic conductivity independently measured for unobstructed liquid directly yields the transport efficiency $\mathcal{B}_k$ discussed in section 3.1.5. Landesfeind *et al* [65] surveyed many specific details about methods by which Macmullin numbers or transport efficiencies can be determined. Using fits of EIS data with transmission-line models, they determined transport efficiencies in a range of porous electrodes and compared these with values calculated from the Bruggemann correlation typically used in DFN models.

3.2.3. Laser diffraction particle size analysis

Laser diffraction particle sizers that can measure the distribution of particle radii within powders are commercially available. Typically they use photodetectors to measure the angle and intensity of light scattered through a sample. The collected pattern is then transformed into a particle-size distribution via the Mie theory of scattering. It is common to describe the spread in size distribution with D_{10}, D_{50} and D_{90} diameters, representing the size at the 10th, 50th and 90th percentiles, respectively. This technique has been widely applied to active-material samples [60, 94, 95]. A flaw of particle-size measurement via laser diffraction is that it assumes scattering from perfect spheres and generally does not provide accurate distributions from the irregularly shaped particles that make up some battery materials [96].

3.2.4. Mercury intrusion porosimetry

Mercury intrusion porosimetry is a destructive technique used to measure porosity, volume of pores, pore size distribution and surface area. In a measurement, increasing pressure is applied to force mercury into smaller and smaller void spaces in the porous medium being studied, and recording the volume of intruded mercury [97].

Smaller pores may not always be fully accessible to mercury intrusion porosimetry, owing to the higher pressures necessary [98]. As such, the method is only suitable for battery electrode coatings with larger pore sizes [17, 19, 99]. It can also be used to measure particle radii within electrodes by exploring the contact

angle, hydrostatic pressure, and surface tension of the mercury [99]. Similar to laser diffraction, the principles of mercury intrusion porosimetry derive from the assumption of perfectly packed spheres [100]. Geometrical parameters for inhomogenous active material particles may be more precisely extracted using imaging methods.

3.2.5. Brunauer–Emmett–Teller adsorption

The Brunauer–Emmett–Teller (BET) adsorption isotherm can be used to measure surface areas within porous media by flushing the pore structure with nonadsorptive gas such as helium, then inducing the adsorption of a surface monolayer of an adsorptive gas, such as nitrogen [101]. Based on formulas derived from the BET theory, the quantity of gas adsorbed correlates with the total surface area of the particles. By tracking the hysteresis of nitrogen adsoprtion and desoprtion, experimental equipment that performs measurements with the BET method can often also be used to infer pore-size distributions.

BET adsorption is a prevalent tool, widely used to extract solid electrode-material surface areas under varying synthesis conditions and degradation/cycling protocols [102–105]. Shortcomings of the technique include the high sensitivity to sample preparation, degassing and lengthy measurement time. BET adsorption cannot deliver very accurate parameters for DFN models, because the technique can only be used on dry powders, and therefore does not characterise the actual areas in chemical contact or available for electron exchange within porous electrodes.

4. Electrode parameters

The anode and cathode active materials undergo redox reactions, contribute towards electron conduction and, most importantly, serve as reservoirs for lithium storage. Typical cathodes comprise transition-metal oxides, such as blends of lithium nickel cobalt manganese oxides, or phosphates, such as lithium iron phosphate (LFP). Anodes typically contain carbonaceous compounds such as graphite, with some incorporating varying amounts of silicon. This section focuses on electrode intrinsic parameters encompassing thermodynamic, kinetic and transport properties, that are independent of pore geometry.

4.1. Parameters

4.1.1. Open-circuit voltage (OCV)

The OCV of a full cell is defined as the potential difference between the positive and negative electrodes when there is no current flow and the cell has relaxed to equilibrium. The OCV is not a constant, but is instead a function of the thermodynamic states of the materials in the electrodes. Generally, the OCV varies significantly with respect to its degree of lithiation (i.e. its SoC), and also slightly with temperature.

To characterise the full-cell OCV, the variation of potential of each of the active materials at equilibrium is measured, both relative to the same reference-electrode reaction [107]—most commonly lithium redox on lithium metal—taking the difference between these two voltages (often termed half-cell OCVs) gives the full-cell OCV. This data can then be supplied to the model either in the form of a look-up table or a suitable mathematical function fitted to the raw data. OCV data is commonly fitted to either (i) functions that are empirical but convenient to work with (e.g. piecewise linear functions [108]), see e.g. [109], or (ii) physically motivated functions [106, 110]. Some of the challenges associated with data-fitting in practice have been discussed by Plett and colleagues [111, 112]. The original modelling work by Newman and co-workers used either a form of the Nernst equation [5] or an empirical expression including hyperbolic tangent terms, exponentials and a constant [6]. Similar approaches have been widely adopted in many other more recent works [44, 113, 114]. Some authors have also fitted a polynomial to the measured data, which may be sufficient for many applications and is simpler to implement [115].

Zhang *et al* [110], Birkl *et al* [106] and Verbrugge *et al* [116] all demonstrated that a realistic function for each half-cell OCV can be derived from first principles using a substitutional lattice gas model. The derivation of these functions is similar to that of a Nernst equation, but is extended to include the energetics of short-range interactions and local equilibria among sites with different energies. The model was demonstrated to accurately represent a wide range of common materials, including graphite, layered nickel-manganese-cobalt oxide, manganese oxide, and iron phosphate. The function is a summation of sigmoidal terms for each plateau in the OCV. Zhang *et al* [110] and Birkl *et al* [106] independently derived an equation for the fraction of sites within the active material occupied by lithium, θ_k, in terms of the OCV, U_k:

$$\theta_k(U_k) = \sum_{i=1}^{N} \frac{\Delta\theta_i}{1 + \exp\left[(U_k - V_{0,i})\, a_i e/kT\right]}. \tag{31}$$

The voltage of each plateau is $V_{0,i}$; the fraction of the SoC range in which the material resides on the *i*th plateau is $\Delta\theta_i$, and a_i is a fitting parameter that approximates the interaction energy between neighbouring ions in the lattice. The expressions used by Zhang *et al* [110] and Verbrugge *et al* [116] are similar to (31), but include a lattice-energy parameter equivalent to the reciprocal of Birkl *et al*'s a_i. Being analytic, (31) is smooth and is therefore apt for use in numerical computations. Unlike the familiar Nernst equation, however, the composition is given explicitly, rather than voltage being an explicit function of the composition. Although expression (31) is generally invertible because θ_k always decreases monotonically with U_k, the inverse function $U_k(\theta_k)$ cannot generally be found analytically, posing a minor implementational inconvenience.

Hysteresis or path dependence effects are usually observed in OCVs, manifesting as a different OCV function being measured during charge, compared to discharge. The reasons for this are widely debated, but generally accepted to be complex and linked to the formation of metastable states within active materials. Hysteresis may be examined using isothermal calorimetry [117], and has been modelled empirically by constructing a differential equation that describes how the hysteresis voltage changes with respect to SoC and history [118].

4.1.2. Stoichiometric limits and electrode balancing

The maximum lithium concentration, $c_k^{\max}$, dictates the extent to which a solid electrode material can incorporate lithium. Materials that can store large amounts of Li per unit weight or volume are generally sought after, since they increase the energy density of the battery. The parameter $c_k^{\max}$ is material-dependent and typically lies between 20 000–55 000 mol m^{-3} for metal-oxide cathodes, and 15 000–35 000 mol m^{-3} for graphitic anodes. This parameter appears in model equation (21), defining the Butler-Volmer reaction rates. Notably, for intercalation compounds that form solid solutions, the exchange current density, j_{k0}, vanishes either when the lithium concentration at the electrode surface approaches its maximum or when it reaches zero.

The theoretical capacity and $c_k^{\max}$ for material *k* may be calculated, through Faraday's law, by using the active material crystal density, ρ_k^{crystal} and the molecular mass of the lithiated active material, m_k. Chen *et al* [19] estimated similar values of $c_k^{\max}$ using both the material coating mass per unit area $M_{\text{coat},k}$ and active material crystal density, through

$$c_k^{\max} = \frac{\rho^{\text{crystal}}}{m_k} \approx \frac{M_{\text{coat},k}}{m_k L_k \varepsilon_{\text{act},k}}. \tag{32}$$

Individual electrodes can typically access maximum and minimum lithium concentrations that lie beyond the capacity ranges accessed in a full cell, as depicted in figure 7. Most positive electrode materials, such as LiCoO$_2$ and nickel-manganese-cobalt oxide, LiNi$_x$Mn$_y$Co$_z$O$_2$ (NMC), undergo irreversible changes of their crystal structure at low stoichiometry, which should be avoided to minimise degradation [119]. Full lithiation of the positive electrode is also not usually possible because cells are fabricated with fully lithiated cathode materials; some capacity is inevitably lost due to the loss of lithium inventory during initial SEI formation. For the negative electrode, it is important to leave some margin to avoid overcharging or overdischarging a cell.
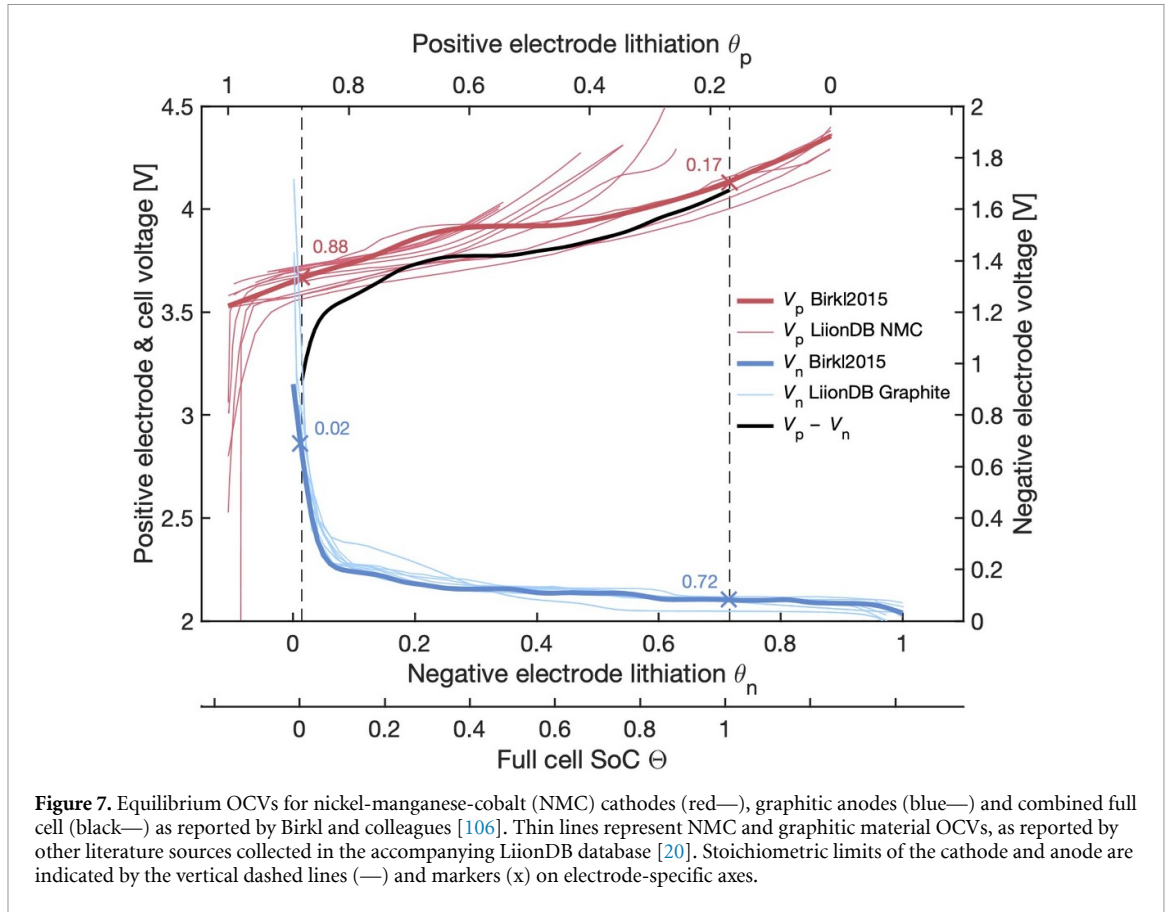
The literature is often unclear whether stoichiometry is defined in terms of (i) a fractional of the cell's SoC (ranging between 0 and 1) that is accessible in practice, but that does not necessarily correspond to concentrations ranging between 0 and c_k^{max}, or (ii) the true theoretical maximum. Adopting a perspective in which lithiation limits are imposed, the fractional SoC, $\Theta(t)$, can be defined as

$$\Theta(t) = \Theta(0) - \frac{A \int_0^t i_{\text{circuit}}(t')\, dt'}{Q_{\text{cell}}}, \tag{33}$$

where Q_{cell} is the capacity of the cell when fully charged (but the anode material may not necessarily be fully lithiated and, likewise, the cathode material may necessarily not be fully delithiated), so that $\Theta > 1$ corresponds to overcharge and $\Theta < 0$ corresponds to overdischarge. Each electrode's state of lithiation can be expressed using a variable ($\theta_k(U_k)$ in equation (31)) which determines the fraction of crystal-lattice sites occupied by Li$^+$. Since $\theta_k(U_k)$ varies in space as well as over time, it is useful to define a volume-averaged counterpart $\langle\theta_k\rangle$:

$$\langle\theta_k\rangle(t) = \frac{\int \theta_k(x,t)\, dV}{V} = \frac{\int c_{ks}(x,t)\, dx}{L_k c_{k,\max}}. \tag{34}$$

Note that c_{ks}, not c_k, is included in (34), because θ_k is a function of the half-cell OCV U_k, which is a function of c_{ks} and not c_k. The full-cell SoC $\Theta(t)$ and the half-cell lithiation fractions, $\langle\theta_n\rangle(t)$ and $\langle\theta_p\rangle(t)$, are linked by

Figure 7. Equilibrium OCVs for nickel-manganese-cobalt (NMC) cathodes (red—), graphitic anodes (blue—) and combined full cell (black—) as reported by Birkl and colleagues [106]. Thin lines represent NMC and graphitic material OCVs, as reported by other literature sources collected in the accompanying LiionDB database [20]. Stoichiometric limits of the cathode and anode are indicated by the vertical dashed lines (—) and markers (x) on electrode-specific axes.

$$\Theta(t) = \Theta(0) + \frac{FA}{Q_{cell}} \left\{ L_p c_{p,max}[\langle\theta_p\rangle(t) - \langle\theta_p\rangle(0)] - L_n c_{n,max}[\langle\theta_n\rangle(t) - \langle\theta_n\rangle(0)] \right\}. \tag{35}$$
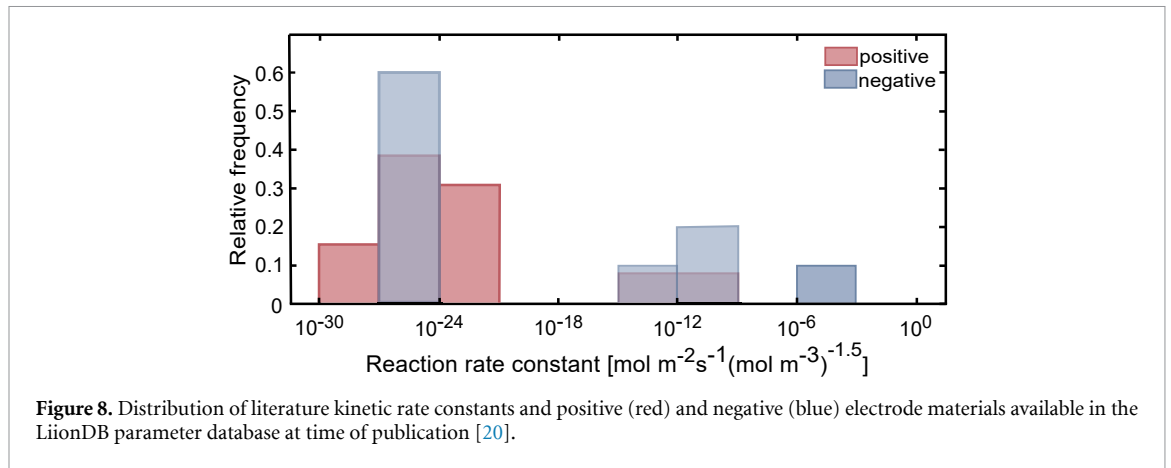
Observe that the electrode-domain thicknesses L_p and L_n appear here. One important use of DFN models is to optimize electrode balancing by illustrating how choices of L_p and L_n affect performance.

Because the full range of individual electrode stoichiometries, $0 < \theta_p < 1$ and $0 < \theta_n < 1$, extends beyond the accessible full-cell SoC range, $0 < \Theta < 1$, full-cell OCV measurements are not sufficient to determine $\langle\theta_k\rangle$; in principle half-cell thermodynamic data from the literature or half-cell measurements with harvested electrodes are also necessary. To match half-cell OCV curves with full-cell OCV data, one can examine turning points in differential voltage measurements [17], perform least-squares regression [99], or implement three-electrode-cell measurements [19, 120]. The initial values of $\langle\theta_k\rangle$ relate to the mass balance between the anode and cathode, the first cycle loss observed during the formation process (usually taking place during manufacturing) and the state of health.

Figure 7 illustrates the range of OCV curves reported in the literature for graphitic anodes and NMC cathodes. There is a lack of consensus between reporting of cell-level SoC, $\Theta(t)$, and materials-level lithiation scales, $\langle\theta_k\rangle(t)$, shown particularly by the variation in lithium stoichiometry and measured half-cell OCV for NMC cathodes. Many papers are careful to distinguish between the full-cell state of charge Θ and electrode stoichiometry θ_k, but some [30, 121, 122] use the term SoC for both, which is confusing for readers trying to parameterise a battery model. figure 7 also highlights an example of electrode stoichiometric balancing, from the work of Birkl *et al* [106], showing how the relative positions of half-cell OCV curves and their minimum/maximum lithiation limits combine to form the full-cell voltage curve.

4.1.3. Butler–Volmer reaction rate constant

Reaction kinetics in porous electrodes are typically taken to follow the Butler–Volmer kinetic equations (20) and (21), which relate the interfacial current density j_k to the surface overpotential η_k. The exchange current density j_{k0}, and hence the reaction rate, is proportional to the Butler–Volmer kinetic rate constant, k_k. A sample distribution of kinetic rate constants for electrode materials reported from the LiionDB parameter database are shown in figure 8. Experimentally obtained exchange current densities vary by several orders of magnitude, with some variation owing to how they are defined [123, 124]. As highlighted by Dickinson and

Figure 8. Distribution of literature kinetic rate constants and positive (red) and negative (blue) electrode materials available in the LiionDB parameter database at time of publication [20].

Wain, this variability may stem from differences in how variables in the Butler–Volmer equation are interpreted by electroanalytical chemists and electrochemical engineers [125]. Differences also arise due to parameter values assumed when processing experimental data, such as effective electrode surface area, discussed in section 3. Caution is advised when comparing published values of j_{k0} and k_k, since the Faraday constant, F, may be omitted from the definition of the interfacial or exchange current densities in some papers, and the effective surface area may not be taken into consideration [5, 44, 126].

Ecker *et al* [17] found that equation (20) was a good fit to exchange current densities measured by EIS for LiNi$_{0.4}$Co$_{0.6}$O$_2$ (NMC406), but not for graphite. Schmalstieg *et al* [99] also found that (20) was a good fit to exchange current densities measured by EIS measurements for NMC811, but the exchange current density had virtually no SoC dependence for graphite. These findings are consistent with SEI-layer properties interfering with the measurements on negative electrodes. Conversely, the same paper by Ecker *et al* [17] found that the Butler–Volmer equation (8) provided a good fit for EIS measurements of charge-transfer resistance on graphite, but not for NMC406. Similarly, Ko *et al* [61] found that k_p extracted from galvanostatic intermittent titration technique (GITT) measurements on NMC111 is not constant, but instead varies with SoC. Recent literature has also suggested that alternative kinetic mechanisms better describe electrochemical reactions at high rates and overpotentials, or with advanced battery formats, such as lithium metal and anode-free cells [123, 124, 127, 128]. A rigorous justification for the common assumption that $\alpha_{ak} = \alpha_{ck} = 0.5$ is also lacking [4, 129], but the factors α_{ak} and α_{ck} are notoriously difficult to measure, though recent developments in nonlinear EIS has shown sensitivity to these reaction symmetry parameters [130]. Deviations in these factors from 0.5 has been used to explain the fact that LiB discharging is faster than charging at a given magnitude of cell voltage [131].
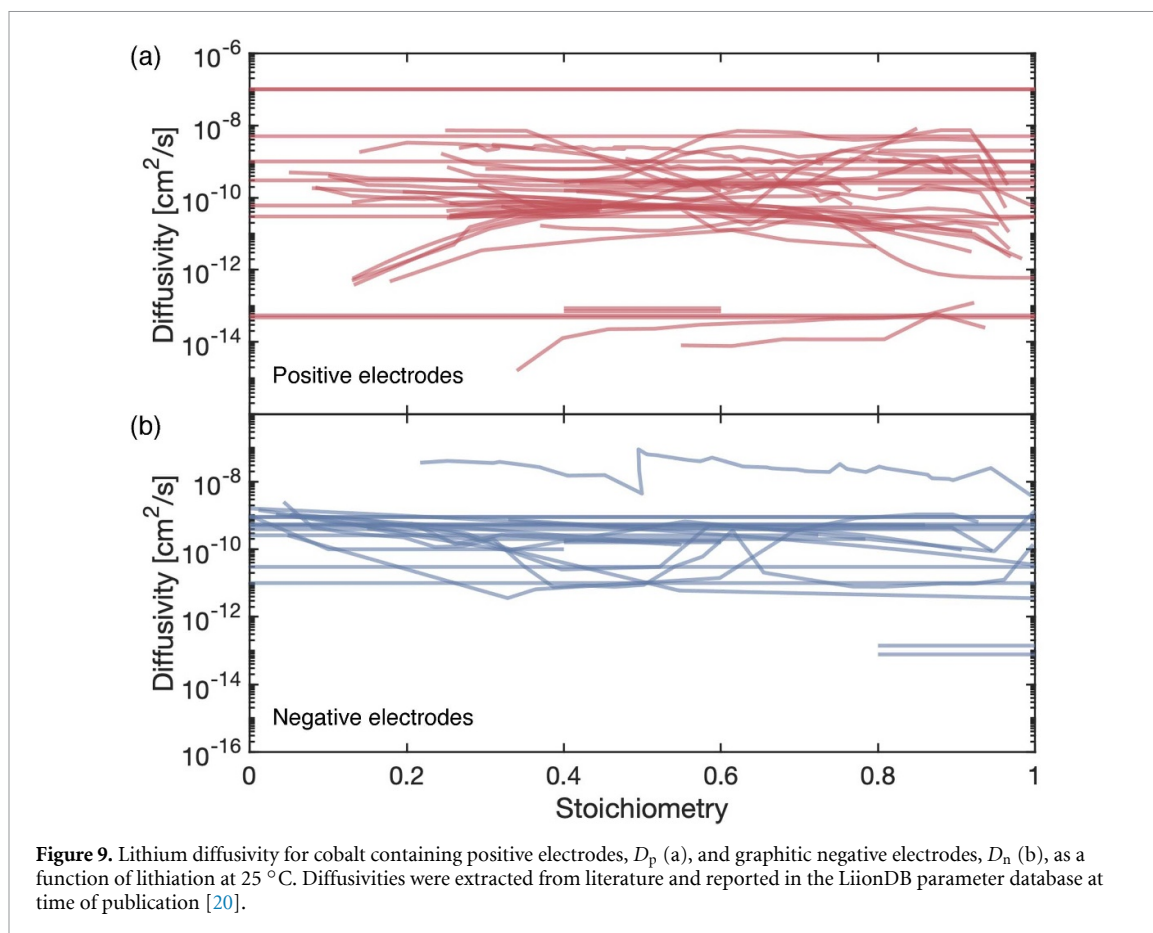
Thermal activation of intercalation kinetics in materials such as graphite and NMC is widely accepted, with Arrhenius relationships assumed between exchange current density and temperature having been reported throughout the literature [17, 19, 99, 132]. Despite being called into question from both theoretical and experimental perspectives, the theory of thermally activated Butler–Volmer kinetics is almost always used in LiB models, for two reasons. First, it requires only two parameters: the rate constant in a reference state, k_k, and associated activation energy. Second, sensitivity analyses [133–135] have shown that DFN models are more sensitive to particle radii, r_k, and diffusivities, D_k, than to reaction kinetics.

4.1.4. Solid-state diffusivity

In the active materials, the Li$^+$ diffusivity, D_k, controls the transport of Li$^+$ within the particles. It becomes very important at high currents, where concentration gradients within the active material may become the main source of overpotential if diffusivities are not large enough. When diffusivities are too small, particle surfaces easily become depleted of or saturated with lithium, which shuts down reaction kinetics and thereby strongly impacts battery operation [133–135].

The first DFN models assumed that solid phase diffusion follows Fick's second law [8], i.e. they used (17) and took D_k to be constant. Studies on parameter identifiability have shown that diffusivity is intrinsically linked to the particle radii, r_k^2/D_k [15, 16]. It should be emphasised that many of the experimental techniques, such as GITT, infer diffusivities under the assumption that a spherical form of Fick's second law applies and so this model assumption would be required for consistency.

Despite the constancy of D_k assumed in the original DFN models, measurements indicate that $D_k(c_k)$ can vary by orders of magnitude, as the Li$^+$ concentration changes [17, 19, 99, 121, 136–139]. The data plotted

Figure 9. Lithium diffusivity for cobalt containing positive electrodes, D_p (a), and graphitic negative electrodes, D_n (b), as a function of lithiation at 25 °C. Diffusivities were extracted from literature and reported in the LiionDB parameter database at time of publication [20].

for positive and negative electrodes in figure 9 show that Li$^+$ typically diffuses through the active materials in the range of 10^{-8} to 10^{-14} cm^2 s^{-1}. For graphite negative electrodes, $D_n(c_n)$ is large for concentrations corresponding to material phase transitions between plateaus on the half cell OCV curve and is small for other stoichiometries. Active materials are typically polycrystalline and both modelling [140] and experimental [141] studies on NMC-type materials agree that diffusion is faster along grain boundaries than within crystals. Cracks form much more quickly during cycling in polycrystalline materials than in single crystal materials, however, causing a further decrease in diffusivity [141, 142]. Nanoscale LFP shows very fast Li-ion transport, but larger LFP crystals have much slower transport, owing to the transport along the rapid b channels becoming blocked by dislocations. Thus, active material quality has a significant impact on battery behaviour.

Concentration-dependent diffusivities have been used in models, which have been shown to match experimental data better at various C-rates and temperatures [17]. They have also been used to investigate how phase changes affect differential voltage signals with and without lithium plating [129]. The temperature dependence of diffusion is well reproduced by an Arrhenius response [17, 139]. While Fickian diffusion is by far the most widely used model of mass transport within particles, there is increasing evidence that other models that account for phase change, such as the Cahn-Hilliard equations [143, 144], may be more appropriate for graphite [145] and LFP [45], although parameters such as the characteristic transition-region length do not have clear meanings in the context of classical thermodynamics.

4.2. Measurement/fitting techniques

4.2.1. Electronic conductivity probes

Four-point surface probes are commonly used to measure the electronic conductivity of porous electrodes. A current is applied across the sample via two of the probes, while the other two measure the potential drop. The probe spacing is fixed, but varies from device to device: it can range from a few micrometers to a few millimeters [146]. By relating the applied current and the measured voltage, the electronic conductivity can be estimated [147, 148], using suitable corrections based on sample size and shape [149]. Current collectors can also be separated from the electrode coating to reduce their influence on measurements by strategies such as the use of strong adhesives to delaminate the electrode material or solvents to dissolve the current

collector foil [19, 71, 150]. Due to the anisotropy of the electrode coatings, conductivity depends on the orientation of the sample [151]. In an operating battery, the through-plane conductivity (in the direction perpendicular to the current collectors) is most relevant for use in the DFN model, as this relates to the movement of electrons from the surface of the electrode particles to the current collector [152]. Bespoke methods have also been developed to measure the combined interfacial resistance [153, 154].

Through-plane conductivity can be measured using a two-electrode method [155, 156]. This involves sandwiching the sample between two probes, then evaluating the direct-current resistance. Deconvolution of contact resistances can be a challenge in the two electrode set-up; bespoke four-point probe designs offer greater accuracy [157].

4.2.2. Pseudo open-circuit voltage (pseudo-OCV) test

During cycling of an active material, the overall voltage response is comprised of the equilibrium OCV of each electrode plus the overpotentials between each electrode and the electrolyte, and the resistive potential difference across the electrolyte and solid components of the electrodes. Each of these contributions to the potentials, except the OCVs, generally increase with current throughput. The galvanostatic pseudo-OCV method minimises the non-OCV contributions by sweeping through a cell's stoichiometric range at a slow rate (e.g. less than C/20—i.e. a current at which the rated capacity of the cell would charge or discharge in 20 h) to determine the cell OCV. It should be noted that this method never truly reaches an open-circuit condition, but can be made to come arbitrarily close to it by decreasing the C-rate. Chen *et al* [19] compared the pseudo-OCV approach to the GITT technique described in section 4.2.3, concluding that polarisation, kinetically stable phase transitions and hysteresis are still observed in most pseudo-OCV data.

4.2.3. GITT

Weppner and Huggins [158] introduced the GITT in 1977 to characterise diffusivities in dense planar electrodes. The method has since been adapted for porous electrodes. GITT involves applying a short and weak current pulse, followed by an open-circuit (no applied current) rest period which is sufficiently long that a cell voltage close to the equilibrium potential is obtained. The charge transferred should be small enough such that the voltage response remains proportional to the current applied, and data should only be processed outside the timescale dominated by capacitive relaxation of the electrolytic double layer. An exemplary set of GITT data is provided in figure 10(a).

For intercalation electrodes, GITT is used to establish electrode OCVs at different states of lithiation [19, 60, 61, 159]. After each current pulse and subsequent relaxation step, the equilibrium OCV, U_k, is given (to a good approximation) by the cell voltage, and the lithiation concentration c_{k0} is known from the pulse current and duration through Faraday's law of electrolysis. It should be emphasized that thermodynamic equilibrium is only well approximated by GITT-derived OCVs that have been recorded with sufficient rest periods after each pulse.

The quantification of the solid-state diffusivity from GITT data is based on an analysis with Fick's second law. Assuming linear diffusion limited by the solid electrode material, and that the pulse duration is short enough that diffusion within the electrode film can be assumed semi-infinite, the diffusivity D_k of lithium within the solid is given by
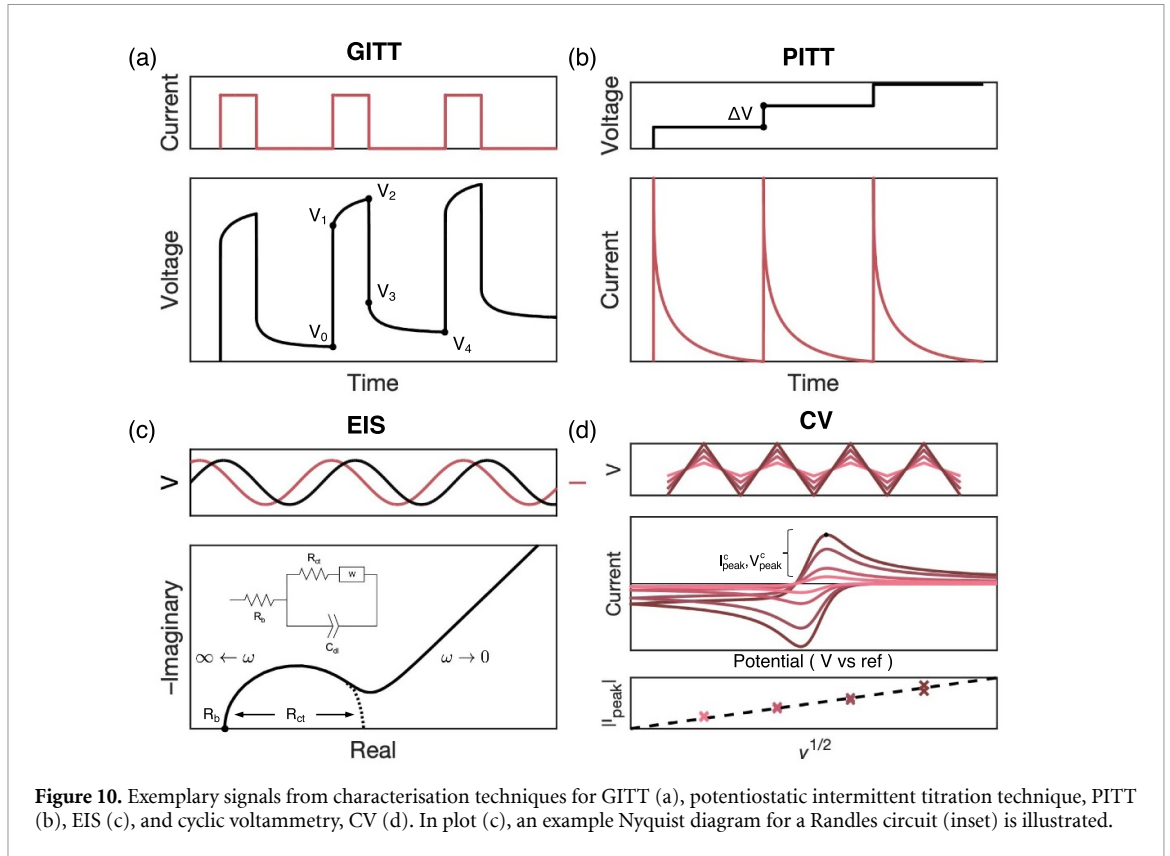
$$D_k = \frac{4}{\pi} \left(\frac{i_{\text{circuit}} A}{S_k F} \right)^2 \left(\frac{U_k'(c_{k0})}{\frac{\partial V}{\partial \sqrt{t}}} \right)^2, \tag{36}$$

where A is the geometrical area of the porous electrode, S_k is the area of the electrode-electrolyte interface within it, c_{k0} is the Li$^+$ concentration in the solid at the beginning of the pulse, $U_k'(c_{k0})$ is the derivative of OCP with respect to concentration at c_{k0}, and $\frac{\partial V}{\partial \sqrt{t}}$ is the derivative of the terminal voltage with respect to the square root of time. Note that this analysis assumes a semi-infinite film penetration model of diffusion [160]; it is important to be aware of whether assumptions concerning the nature of diffusion are applicable to the system being studied [132].

The GITT method was originally derived for compact thin-film electrodes [158], but remains valid for porous electrodes, as long as S_k is taken to be the effective surface area available for charge transfer within the porous material and the configuration is such that spherical diffusion within the electrode particles does not become rate limiting. Generally, S_k relates to the DFN surface-to-volume parameter b_k, through

$$S_k = b_k A L_k, \tag{37}$$

where L_k is the thickness of the porous electrode. Assuming that the electrode comprises spherical particles, all of radius r_k, that occupy a volume fraction $\varepsilon_{\text{act},k}$ of the active material, and that the distribution of

Figure 10. Exemplary signals from characterisation techniques for GITT (a), potentiostatic intermittent titration technique, PITT (b), EIS (c), and cyclic voltammetry, CV (d). In plot (c), an example Nyquist diagram for a Randles circuit (inset) is illustrated.

particles throughout the film depth is uniform then, it follows that $b_k = 3\,\varepsilon_{act,k}/r_k$. Application of GITT to porous-electrode models is well detailed by Nickol *et al* [161].

A reaction-kinetic overpotential is present during any galvanostatic measurement, hence the GITT set-up should be chosen to minimise any overpotentials observed on the working electrode, maintaining accurate measurement of the thermodynamic states through the OCV. In two-electrode measurements care should be taken to ensure that these overpotentials are small enough that they do not appreciably contaminated the results. Even when using Li metal counter electrode half cells, the Li metal may contribute an additional overpotential, leading to inaccuracies in the observed cell voltages and underestimation of diffusion properties. Three- or four-electrode cells, incorporating one or two reference electrodes, produce more accurate voltage responses because they allow the contributions from the overpotential to be quantified and subsequently subtracted off of the data [161].

For sufficiently small currents and short time intervals, $dV/d\sqrt{t}$ is constant, experimental data can be used to estimate the change in OCV and the charge injected with the pulse directly relates to the concentration change in the solid through Faraday's law of electrolysis. Thus, one can use voltages from the data in figure 10(a) to simplify equation (36), yielding

$$D_k = \frac{4}{\pi\tau}\left(\frac{r_k}{3}\right)^2\left(\frac{V_4 - V_0}{V_2 - V_1}\right), \tag{38}$$

where, apart from the measured voltages V_j, the only inputs are the particle radius, r_k, and the pulse duration, τ. This approach removes some error associated with overpotentials, since the equilibrium voltage is recorded without an internal resistance contribution. Poor estimates of diffusivity can still occur, however, particularly when GITT is undertaken in an SoC region with a relatively flat OCV response, or if equilibrium is not (approximately) reached by the end of each rest period. GITT measurements directly parameterise the diffusional time constant, r_k^2/D_k, with the extracted diffusivity having an inherent dependence on the measured radii r_k^2. This link also makes it difficult to interpret GITT results for electrodes with a wide range of particle sizes. An alternative approach is to fit the voltage transient versus $\sqrt{t}$ during the current pulse, and calculate the diffusion coefficient directly using equation (36). This approach does not eliminate any overpotential errors. More elaborate methods to calculate S_k can be used, as described in section 3, but the value should always be consistent with that used in the DFN model.

Recently, there have been several developments in the application and analysis of this technique. A modified GITT technique, using a 'staircase' current profile, has been reported to determine other kinetic

parameters, including the exchange current density and charge transfer coefficients, by fitting the observed overpotentials to a modified Butler-Volmer equation [162]. Lacey and colleagues have also modified the GITT technique to reduce experimental time and provided validation based on DFN model simulations [163, 164]. Other developments in the estimation of diffusion coefficients have focused on the methods to fit the model to the data [161, 165, 166].

4.2.4. Cyclic voltammetry

Cyclic voltammetry (CV) is a technique commonly employed to investigate reduction and oxidation processes [160, 167], using a three electrode system—working, counter and reference electrodes—and measuring the current response to a linearly cycled potential sweep between two given voltage limits, as depicted in figure 10(d). In sweep voltammetry, an applied potential is varied linearly with time while recording the resultant current. This potential sweep is characterised by a particular scan rate, ν (with units V s^{-1}). Data is typically reported in the form of a cyclic voltammogram, which plots current versus voltage, both parametric functions of time. Analysis of cyclic voltammograms provides both qualitative and quantitative information about electrode reaction kinetics and mass transport. For electrode parameterisation, CV can be used to obtain kinetic rate constants of (de)lithiation [168, 169] and the diffusion coefficient of lithium within electrodes [170]. These techniques are discussed in detail in Kim *et al* [171].

The quantitative analysis of cyclic voltammograms varies according to whether the electrochemical reaction is classified as reversible (i.e. kinetically fast), quasi-reversible, or irreversible (i.e. kinetically sluggish). For a reversible reaction, the forward and reverse electron-transfer steps are in equilibrium and voltage follows a Nernst-like equation. Li-ion intercalation is often considered to be reversible [172], though quasi-reversible analyses have also been applied when rates of charge transfer and mass transport are similar [173]. Given a diffusion-controlled, reversible single-electron transfer process, the peak current is proportional to the square root of the scan rate ($I_{peak} \propto \sqrt{\nu}$).

For porous electrodes, the surface area and morphology of the surface also affects the shape of the voltammogram. As many common models that underpin CV analysis are derived based on assumptions that the working electrode is small compared to the counter and that liquid-phase diffusion is semi-infinite, translation of the theoretical equations to represent porous electrodes is difficult. The effects on peak voltage and reversibility are particularly pronounced on thicker porous electrodes [173]. The impacts of intercalation-particle geometry and dispersion on CV profiles have also been modelled [169]. It was found that accounting for the real particle-size distribution may be crucial for determining the voltammetric response. When mass-transfer contributions derive from both free electrolyte adjacent to the electrode and pore-filling electrolyte within it, reversible reactions may also produce an apparent shift in peak voltage position, proportional to the scan rate [173].

In general, thin electrode coatings minimise the observed kinetic limitations and the effect of the porous electrode geometry. Given a reversible CV response, the relationship between the peak current, I_{peak}, and the scan rate, ν, see figure 10(c), can be fit with the following equation to elucidate the solid-phase diffusivity of lithium, D_k [160, 173, 174]:

$$I_{peak} = 0.4463 \, Fc_k S_k \sqrt{\frac{F\nu D_k}{RT}}. \tag{39}$$

Here c_k is the concentration on the surface of the particle and S_k is the effective surface area per unit mass. The effective surface area can be further refined to account for the electrochemically active surface area. Since practical battery electrode materials more often exhibit quasi-reversible or irreversible characteristics, CV parameterisation techniques may only offer qualitative comparisons between effective kinetic and transport properties.

4.2.5. Potentiostatic methods

Potentiostatic methods involve applying a voltage step and observing the current response. Examples include a voltage sweep, such as in CV, or constant voltage measurements, such as chronoamperometry. Chronoamperometry can also be applied over a range of concentrations or states of charge of the electroactive material and, at each concentration (or voltage), the current transient can be used to calculate the solid-state diffusion coefficient.

In the potentiostatic intermittent titration technique (PITT), a stepped constant voltage is applied and the current decay is tracked, at each voltage, to a set current limit. A rest period can also be introduced in between each voltage step, after the current decays such that OCV is (approximately) reached [175, 176]. The exclusion of rest periods accelerates data collection. However, including the rest period in PITT means the titration method can be used to calculate the diffusion coefficients while minimising overpotentials that

contribute errors to the concentration estimation. Care must be taken with any overpotential observed in the measurement and, again, 3-electrode measurements with a reference electrode are significantly more accurate. A typical PITT data set is depicted schematically in figure 10(b).

A model based on Fickian diffusion is used to estimate diffusivity from current data [176]. In the case where $t \ll r_k^2/D_k$ (short times compared to the time scale of solid-state diffusion), and where interfacial reaction kinetics is reversible, it is appropriate to apply the Cottrell equation [160]:

$$D_k = \pi t \left(\frac{i(t)}{FS_k(c_{ks} - c_{k0})} \right)^2, \tag{40}$$

whereas for $t \gg r_k^2/D_k$ (long times) the current decay becomes exponential and the solid-state Li diffusion coefficient can be determined from [176, 177]:

$$D_k = -\frac{4}{\pi^2} \frac{r_k^2}{\partial t} \frac{\partial \ln i}{\partial t}. \tag{41}$$

This has been expressed in terms of a particle radius, r_k, and, within the caveats described in section 4.2.3, it is true to say that $b_k = 3\,\varepsilon_{act,k}/r_k$.

Malifarge *et al* [178] have provided guidelines for the implementation of PITT and its underlying assumptions. Less conventionally, PITT can also evaluate the exchange current density [179] but, as already mentioned (section 3.2.2), EIS is more often used. Diffusion coefficients via PITT and GITT have been shown to corroborate one another [180, 181]. The potentiostatic methods offer a speed advantage over galvanostatic methods, but additional measures may be needed to minimise the potential difference between the working electrode and the reference or counter electrode, and the voltage drop across the electrolyte. Not properly accounting for these overpotentials can lead to overestimates of the solid-phase diffusion coefficients.

4.2.6. Electrochemical impedance spectroscopy

The EIS technique was described in section 3.2.2 of this review and is revisited again in section 5.2.1. In the context of electrode parameterisation, EIS may be used to estimate charge-transfer resistance, double-layer capacitance and diffusion timescales, usually by fitting parameters of a simple circuit model to EIS data, by means described below and further detailed in [17, 33, 168]. A typical model is the Randles circuit which, per electrode, consists of a double-layer capacitance in parallel with the series combination of a Warburg element, representing diffusion, and a charge-transfer resistance, as shown in figure 10(c). Further series resistances may be added to represent additional ohmic and ionic voltage drops, as well as additional elements to represent electrolyte dynamics, if required.

4.2.6.1. Charge transfer

An expression for charge-transfer resistance may be derived by linearising the Butler-Volmer equation (20) for small values of the overpotential, i.e. about $\eta_k = 0$. On doing so, one finds that the charge transfer resistance (per electrode), R_{ct}, relates to exchange current density through:

$$j_{k0} = \frac{RT}{S_k F R_{ct}} = \frac{RT}{AL_k b_k F R_{ct}}. \tag{42}$$

Measurements of R_{ct} by EIS have thus been used to determine kinetic parameters [93, 182].

Large variances among calculated exchange current densities j_{k0} stem, in part, from the choice of surface area, with different groups using different definitions, as described by Chang *et al* [183] and Koch [184]. The exchange current density relates to the Butler–Volmer rate constant, k_k, through equation (21).

The identification of the R_{ct} value associated with the main intercalation reaction for individual electrodes is a challenging task. Without a reference electrode, it is not possible to distinguish between the separate half-cell reactions (recall that in the model, there are in fact two Butler-Volmer equations, one for each electrode). Another issue is that the impedance response of the active materials and the response associated with the constantly evolving passivation surface films tend to occur in similar frequency ranges [185]. Changing porosity and surface roughness also leads to frequency dispersion [186]. The majority of strategies to fit R_{ct} from overall spectra involve performing EIS measurements under conditions that cause the kinetic and surface-layer behaviour to diverge. This includes observing dependence on temperature [19], changes with conditioning cycles to develop SEI [187], or varying SoC [188]. Insight can also be gained by comparing EIS spectra obtained from full-cell and half-cell configurations [99]. Non-linear EIS has been implemented to analyse higher-order harmonics [130]. The temperature dependence of R_{ct} has been modelled in terms of the activation energy for lithium transport through the SEI layer [189].

4.2.6.2. Diffusion

While charge transfer occurs at medium to high frequencies, the low-frequency EIS response of a porous electrode provides information about the solid-state diffusion coefficient in each electrode [190]. The considerations mentioned above also apply here, namely that, without a reference electrode, it is not possible to distinguish between the separate electrodes (note that this issue is not unique to EIS, it also applies to GITT and other techniques mentioned in this section). In the frequency domain, diffusion transport is characterised by a Warburg element, which may be derived for various different geometric configurations, including thin films, as well as planar, cylindrical, or spherical particles (see Song and Bazant [191]). For spherical particles, the diffusion-related impedance for each electrode k may be expressed as [16]:

$$Z_{\text{diff,sp,k}} = U_k'(c_{k0}) c_k^{\max} \frac{\tau_k^d}{3Q_k} \frac{\tanh\left(\sqrt{s\tau_k^d}\right)}{\tanh\left(\sqrt{s\tau_k^d}\right) - \sqrt{s\tau_k^d}},$$ (43)

where s is the Laplace variable, $U_k'(c_{k0})$ is the gradient of half cell OCV, with respect to concentration, τ_k^d is a diffusion timescale r_k^2/D_k for each electrode, and $Q_k = FAL_k\varepsilon_{\text{act},k}c_k^{\max}$ is the maximum capacity of each electrode.

Levi and Aurbach [136] demonstrated good agreement between the diffusivity values obtained by PITT and EIS. Ecker *et al* [17] demonstrated good agreement between the diffusion values obtained by GITT and EIS, except for the highly lithiated phases of graphite in which too few EIS measurements were taken to identify the spikes in D_n corresponding to the phase transitions. Further comparison of the techniques for characterising diffusion coefficients can be found in Deng and Lu [192] and Ivanishchev *et al* [193]. Applying titration techniques for SoC-dependent diffusivities is also particularly time-consuming (ca. 17 days [194]) and EIS may be a more time-efficient alternative. Similar to most parameters with Arrhenius-like responses, the activation energy can be determined by fitting repeat measurements at different temperatures [17, 99].

5. Electrolyte parameters

Intrinsic electrolyte properties that parameterise DFN-type models are primarily concerned with how ionic and neutral species in solution are redistributed under the influence of electric fields, concentration (electrochemical potential) gradients and bulk convection. Transport properties are sensitive to salt and solvent composition, as well as temperature.

Ion transport within the electrolyte for DFN models was originally described using multi-component concentrated solution theory [5, 14, 195, 196]. As such, the three familiar transport properties of ionic conductivity, σ_e, salt diffusivity, D_e, and transference number, t_+^0, are related to a set of three pairwise Stefan–Maxwell diffusivities, which account for frictional drag between solvent and cation, solvent and anion, and cation and anion, respectively. Dilute-solution theory has also been applied in the literature, to model the electrolyte phase in batteries [17]. Key assumptions made for this approach include non-interacting ions, infinitely dilute salt concentration and thermodynamic ideality $(1 + \partial \ln f_\pm / \partial \ln c_e = 1)$. Bizeray *et al* [197], as well as Richardson *et al* [198], review the discrepancies between dilute, moderately-concentrated, and concentrated models. In typical battery applications, concentrated electrolytes are used, and concentrated solution theory is better suited to describe the underlying physics, as well as to model a broad range of scenarios such as fast charging or complex multi-component electrolytes.

When parameterising electrolytes for as-received commercial cells, manufacturer data sheets at the time of assembly may be used when available, or samples will need to be extracted and characterised—for example with centrifuge and spectroscopy [199]—to determine the exact formulation to study. Electrolyte composition is known to vary throughout the life of a cell as salt and solvent are consumed by side reactions [199].

5.1. Parameters

5.1.1. Ionic conductivity

The ionic conductivity, σ_e, quantifies the mobility of ions under an electric field, in the absence of concentration gradients. It appears in the generalised Ohm's law (equation (4)) and determines the ionic current in response to the gradient of the electrochemical potential. Ionic conductivity is a strong function of temperature and concentration. In dilute electrolytes, conductivity rises with salt concentration, as the number of mobile ions in solution increases. As salt content increases past a certain threshold, however, species–species interactions, such as ion pairing, cause σ_e to fall [200]. The dependence of conductivity on salt concentration at a given temperature can be fit well with simple polynomial forms [201] or by phenomenologically inspired forms, such as the square-root dependence of equivalent conductance
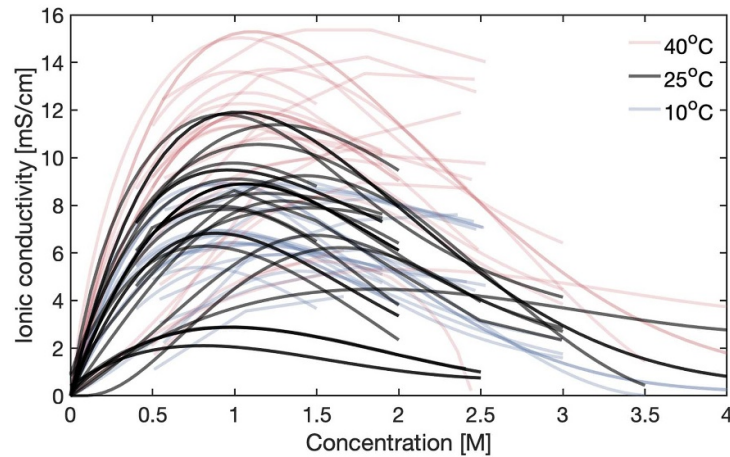
Figure 11. Ionic conductivities of LiPF$_6$-containing electrolytes, at temperatures of 10 °C (blue), 25 °C (black) and 40 °C (red), reported from the LiionDB literature parameter database [20].

$(\sigma_e/(Fc_e))$, predicted by Debye–Hückel limiting behaviour [202–204]. Other empirical functional forms have also been employed, to account for temperature dependence [205, 206].

Ionic conductivities, σ_e, for a variety of LiPF$_6$-containing electrolytes from the property database are presented in figure 11. Generally, ion transport improves with temperature. The temperature dependence of electrolyte conductivity in practical conditions is well-described by a simple Arrhenius relation [17, 200]. Consistent results may be attained by interpolating conductivities using activation energies fit from a range of temperatures. Extrapolating to wider temperature ranges may require compensating for thermal effects on the dielectric constant and viscosity [207, 208].

In LiBs, the electrolytic solution permeates porous phases in the separator and electrodes. Therefore, before they can be utilised in the DFN model, effective transport parameters must be obtained by scaling with a transport efficiency factor, $\mathcal{B}$. These extrinsic details were discussed in section 3.1.5.

5.1.2. Salt diffusion coefficient

The salt diffusivity, D_e, determines the contribution to the ionic flux by salt concentration gradients, as given by equation (2). The thermodynamic diffusivity, $\mathscr{D}$, also describes diffusion under the true driving force of chemical potential gradients [196]. A direct conversion between $\mathscr{D}$ and D_e—the value usually experimentally measured—exists via the thermodynamic factor, $1 + \partial \ln f_\pm / \partial \ln c_e$ (discussed below in section 5.1.4):

$$D_e = c_T \overline{V}_0 \left(1 + \frac{\partial \ln f_\pm}{\partial \ln c_e} \right) \mathscr{D}. \tag{44}$$

The additional term, $c_T \overline{V}_0$, which is the total molarity, c_T, multiplied by the solvent partial molar volume, $\overline{V}_0$, arises as a drift factor that puts D_e in reference to the solvent velocity. It is this diffusion coefficient, D_e, which most commonly appears in DFN model equation (2). Diffusion coefficients have been demonstrated to decrease with increasing salt concentration and solvent viscosity, as measured by a range of techniques. The rate of diffusion also increases with temperature. Figure 12 shows the salt diffusivities, D_e, reported in the literature across varying solvent compositions and salt concentrations. Diffusion coefficients are typically well fitted by simple polynomial expressions or exponentials.

Salt diffusion coefficients can be measured experimentally (see restricted diffusion below, in subsection 5.2.2, [204, 209]). Models that use a constant, average diffusivity will inherently force concentration gradients in solution to develop symmetrically [210]. This may cause an over- or underestimation of the concentration polarisation. Many modeling efforts use approximate diffusion coefficients. Schmalstieg *et al* [99] use the Nernst–Einstein relationship, derived from ideal, infinitely dilute assumptions, to estimate D_e from σ_e. The Nernst-Einstein model is not well justified for concentrated solutions, however, and deviations from this ideal behaviour occur well below the salt concentrations of around 1 M that are typical in LiB electrolytes [197]. Self-diffusivities attained by nuclear magnetic resonance (NMR) or molecular dynamics, while similar in magnitude to D_e, require additional interpretation to be used consistently in the DFN model [211, 212].

The choice of model used to extract the diffusion coefficient from experimental data strongly influences the inferred diffusivity. For example, following Fuller *et al* [6], the ion flux (equation (2) in our macroscopic
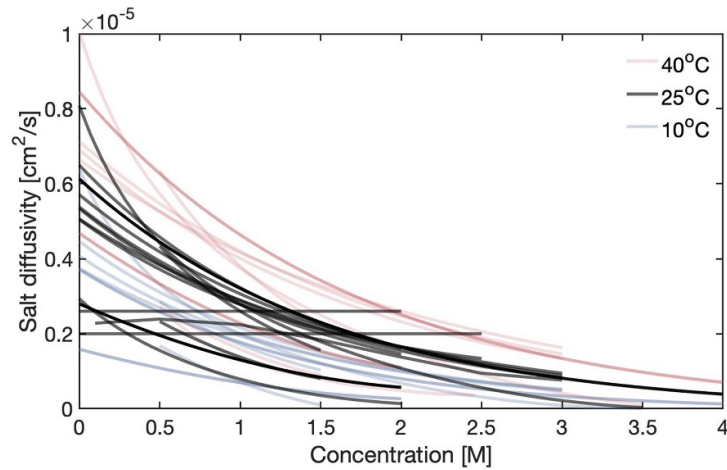
Figure 12. Salt diffusivities of LiPF$_6$-containing electrolytes, at temperatures of 10 °C (blue), 25 °C (black) and 40 °C (red), reported from the LiionDB literature parameter database [20].
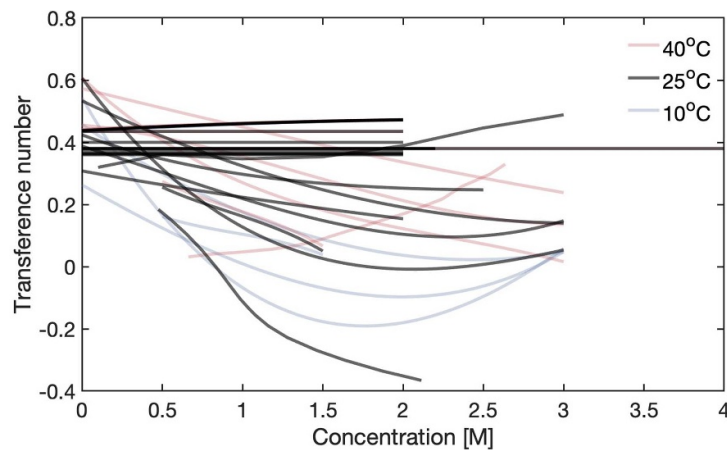

Figure 13. Transference numbers of LiPF$_6$-containing electrolytes at temperatures of 10 °C (blue), 25 °C (black) and 40 °C (red), reported from the LiionDB literature parameter database [20].

relationships) is composed of contributions from migration and diffusion, with convection assumed to be negligible. The majority of DFN battery models have adopted this convention. Indeed, if convection, driven by the density changes which accompany concentration changes, is accounted for, as discussed by the works of Liu and Monroe [213, 214], this may skew the apparent diffusion coefficient and transference number.

5.1.3. Transference number
The transference number, t_+^0, is the fraction of the conductivity contributed by cation motion. This parameter is typically reported relative to a reference frame set by the solvent velocity, which is taken to be zero in conventional DFN models. Cation and anion transference number must sum to unity. From figure 13 it is clear that the lithium ion carries a minority of the charge during typical battery operation. Many battery models choose to use a simplified average t_+^0 value in the 0.3–0.4 range.

A low transference number implies poor power efficiency. Diederichsen *et al* [215] demonstrated, via a sensitivity analysis on the DFN model, that raising the transference number by 0.2 can have significant impact on accessible capacity during charge and discharge. The limiting current—the maximum current at which charge carriers are completely depleted at an electrode—is also a strong function of transference and diffusivity.

While it is clear that accuracy of the transference number has a strong impact on the accuracy of battery models at high C-rate, consensus is low on the expected magnitudes and composition dependencies of t_+^0. The varied experimental approaches and processing techniques, using dilute or concentrated solution theory, as discussed in section 5.2, also contribute to the spread in the data across all electrolyte formulations and salt compositions [216]. For example, experimentally obtained negative cation transference numbers have

been rationalised by the presence of charged or neutral aggregates [217], or by moving boundaries due to lithium plating [218]. The choice of reference velocity (e.g. solvent or volume-averaged) used can also impact apparent transference [196, 213].

The ultimate purpose of these electrolyte parameters is to predict the lithium ion concentration, as a function of position and time. It is important to reiterate that the specific formulation of a DFN model will impact the interpretation of experiments designed to measure t_+^0. For example, models that incorporate dendrite growth [219] will predict vastly different transference numbers to models with ion pairing [218]. Similarly, models that do not include solute-volume effects [213] will overpredict transference when convective-polarisation suppression is wrongly accounted for as a migration effect [204, 209]. Finally, it should be borne in mind that, at low C-rates, simplifying assumptions about t_+^0 have minimal impact on simulation validity, but that these assumptions may be violated at higher C-rates.

5.1.4. Thermodynamic factor
The thermodynamic factor, $(1 + \partial \ln f_\pm / \partial \ln c_e)$, is key to translating a concentration difference into an OCV drop, as can be seen from the generalised form of Ohm's law in equation (4). Thermodynamic factors measure solution non-ideality, accounting for deviations from Nernstian behaviour. The thermodynamic factor is a grouping of terms which arises when the derivative of the chemical potential, μ_e, with respect to concentration, is computed [195]. This leads to the appearance of the derivative of the mean molar salt activity coefficient, $f_\pm$, with respect to salt molarity, c_e. In the literature, the gradient of the activity coefficient is also often defined relative to composition in a molal (m_e) basis, which can be mapped from the molar basis via the mean molal activity coefficient, $\gamma_\pm$, solvent molarity, c_0, and partial molar volume of solvent, $\overline{V}_0$:

$$1 + \frac{\partial \ln f_\pm}{\partial \ln c_e} = \frac{1}{c_0 \overline{V}_0} \left(1 + \frac{\partial \ln \gamma_\pm}{\partial \ln m} \right) = \frac{1}{RT} \frac{\partial \mu_e}{\partial \ln c_e}. \tag{45}$$

By definition, the thermodynamic factor approaches unity at infinite dilution. Debye-Hückel theory predicts a decrease in thermodynamic factor with respect to concentration near infinite dilution [202, 203, 220], but this concentration range is far from the practical concentrations used in lithium-ion electrolytes. The LiB literature, which focuses on moderately dilute to concentrated electrolytes, typically reports $1 + \partial \ln f_\pm / \partial \ln c_e$ values above unity that increase across the observed concentration range, in agreement with a condition where ion–solvent or ion–ion interactions are significant [209]. There also appears to be a weaker dependence on temperature than for other parameters [206]. Polynomials or power series in $\sqrt{c}$, following Debye-Hückel theory, have been used to fit correlations for $1 + \partial \ln f_\pm / \partial \ln c_e$ [204, 209].

The measurements summarised in figure 14 indicate that conventional lithium-ion electrolytes with compositions above 0.5 M should not be treated as ideal [206, 209, 221]. The original DFN publications included $1 + \partial \ln f_\pm / \partial \ln c_e$ in their model formulation, but assumed ideality because thermodynamic data was unavailable [5, 6]. Many subsequent DFN models for conventional LiBs have dropped $1 + \partial \ln f_\pm / \partial \ln c_e$ [17, 19, 99]. Inspection of the DFN model formulation reveals that neglect of the thermodynamic factor has no effect on compositions predicted by equations (1) and (2), but exclusion of $1 + \partial \ln f_\pm / \partial \ln c_e$ will introduce errors in the concentration overpotential, as seen in equation (4). In modelling, this will impact predicted battery capacity, due to the propensity to underpredict cell-voltage cutoffs during charge/discharge. Ideal assumptions only have a strong influence at medium-high C-rates, however, when ohmic losses are not dominant. In situations where battery operation induces a high degree of concentration polarisation, or for cell formulations with particularly high electrolyte molarities, inclusion of an accurate $1 + \partial \ln f_\pm / \partial \ln c_e$ is warranted.

5.1.5. Partial molar volumes
Partial molar volumes are thermodynamic properties that describe how volume is distributed across the components in solution ($\overline{V}_e$ for salt and $\overline{V}_0$ for solvent). Doyle *et al* [5] simplified their treatment of concentrated solution theory by ascribing zero molar volume to the dissolved salt in solution. Partial molar volumes have since been included in DFN-type models [201, 209, 213, 222].

In the one-dimensional ion conservation equation (1), the divergence of flux $\frac{\partial N_e}{\partial x}$ yields an excluded-volume factor $\left(1 - \frac{d \ln c_0}{d \ln c_e} \right)$. As solvent molarity c_0 is typically a weak function of salt content, c_e, in typical lithium-ion electrolytes, Newman [195] use this assumption to neglect the excluded-volume factor, hence setting $\overline{V}_e$ to zero. Partial molar volumes relate to the excluded-volume factor through the solvent concentration, c_0, and solution density, ρ [195]:

$$1 - \frac{d \ln c_0}{d \ln c_e} = \frac{\rho}{c_0 M_0} \left(1 - \frac{d \ln \rho}{d \ln c_e} \right) = \frac{1}{c_0 \overline{V}_0}, \tag{46}$$
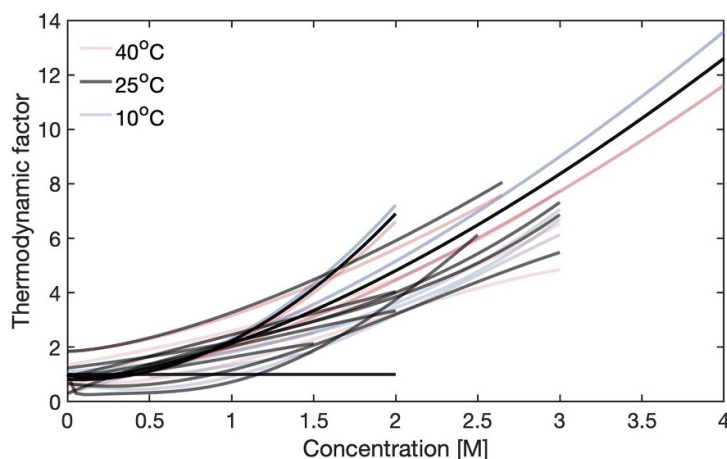
Figure 14. Thermodynamic factors of LiPF$_6$-containing electrolytes at temperatures of 10 °C (blue), 25 °C (black) and 40 °C (red), reported from the LiionDB literature parameter database [20].

with M_0 being the solvent molar mass. One can measure $\overline{V}_e$ and $\overline{V}_0$ readily with densitometry, as discussed in section 5.2.5. Recent spectroscopic techniques have also allowed for the probing of solvent concentrations [223, 224].

5.2. Measurement/fitting techniques

5.2.1. EIS
We have previously discussed the use of EIS in inferring geometrical and electrode intrinsic parameters in sections 3.2.2 and 4.2.6, respectively. Here, we cover its use for elucidating electrolyte intrinsic properties. Commercially-available conductivity probes which operate on frequency-based principles are commonly used to measure ionic conductivities for many common lithium-ion electrolyte formulations [200, 201, 205, 209, 225–227].

EIS is also performed with symmetric planar cells with blocking (stainless steel) or non-blocking (lithium) electrodes. The ionic conductivity, σ_e, may be extracted by measuring the high-frequency resistance value, R_b, in the bulk electrolyte, relative to the EIS cell geometry, and then leveraging the equation:

$$\sigma_e = \frac{L_s}{R_b A}, \tag{47}$$

where L_s is the planar inter-electrode spacing and A is the geometrical electrode area. This is often done with an electrolyte soaked porous separator between electrodes and can be used to calculate the effective conductivity, based on the high frequency bulk resistance intercept on a Nyquist plot [204, 228, 229]. The low-frequency impedance response can also determine contributions from the ionic diffusion coefficient, $D_e(c_e)$, and transference number, $t_+^0(c_e)$ [228, 230]. This approach is akin to a frequency-domain analysis of repeated polarisation-relaxation experiments, discussed in the following section.

5.2.2. Polarisation-relaxation cells
Polarisation-relaxation cells refer to symmetric planar lithium metal electrode cells, used to characterise electrolyte properties by performing a sequence of steps where a current or voltage (or lack thereof) is applied. The concentration gradients resulting from polarisation-relaxation steps are then tracked, often being inferred through concentration overpotentials (also called diffusion potentials), which scale with the concentration gradient [197]. The next few sections outline common polarisation-relaxation experimental techniques used for electrolyte parameterisation.

5.2.2.1. Restricted diffusion
The electrolyte salt diffusion coefficient, $D_e(c_e)$, is best measured with a restricted-diffusion experiment in a sealed vertical cell, where the ion flux directly opposes the direction of gravity. Orientation is important, especially when no porous separator is employed to prevent natural convection [195] or buoyancy effects [231] from marring the method. During restricted diffusion, a nonuniform concentration profile is induced across an electrolyte, often galvanostatically or potentiostatically, before monitoring the relaxation of the concentration difference between two fixed points. As concentration gradients relate to the OCV via

equation (4), the diffusion coefficient can be inferred from the exponential relaxation of the cell voltage [196, 204–206, 209, 232]:

$$\ln V_{\mathrm{OCV}} \propto \Delta c_{\mathrm{e}} = -\frac{\pi^2 D_{\mathrm{e}}^{\mathrm{effective}}}{L_{\mathrm{s}}^2} \cdot t + \mathrm{const,} \tag{48}$$

where V_{OCV} is the restricted diffusion cell voltage measured during the open-circuit relaxation, Δc_{e} is the difference in concentration between the points where V_{OCV} is measured, L_{s} is the separator or bulk electrolyte thickness and t is time. A formal analysis by Newman and Chapman [196] showed that this linear time dependence of the logarithm of voltage can be used to process data accurately, even when diffusivity varies with respect to concentration. Thus, when concentration differences are sufficiently small, Fickian diffusion with a constant diffusion coefficient can be assumed and the diffusivity resulting from a restricted-diffusion measurement should be interpreted as the value at the electrolyte's equilibrium concentration.

Ehrl *et al* [233] found that the restricted-diffusion method through steady-state polarisation and long-term relaxation was less susceptible to the influence of double-layer relaxation effects than pulse-polarisation methods. Error due to surface effects may also be avoided by using a four-electrode cell, containing two reference electrodes positioned at some distance from the reactive metal interfaces, to track diffusivities using cell voltages, as presented by Farkhondeh *et al* [234].

When performing restricted diffusion measurements, one should ensure that the inter-electrode length, L_{s}, between electrodes and duration of voltage relaxation, t, are such that the voltage relaxes linearly. Other indicators of composition such as conductance and spectroscopic response can also been used to track concentration gradients between two points [196, 221, 235, 236].

5.2.2.2. Galvanostatic polarisation

The galvanostatic polarisation, or current interrupt method, originally implemented by Ma *et al* [7] for polymer electrolytes, can be used to measure the transference number. This analysis is based on semi-infinite linear diffusion [160], where the concentration gradient or OCV measured immediately after a galvanostatic pulse is directly related to the transport and thermodynamic properties of the electrolyte. By varying the polarisation time, t_{i}, and current density, i_{circuit}, the slope, m, of cell potential, V, after the moment of current cutoff with respect to a transformed time variable $i_{\mathrm{circuit}} t_{\mathrm{i}}^{1/2}$, can be related to the transference number via:

$$t_+^0 = 1 - \frac{mFc_{\mathrm{e0}}\sqrt{\pi D_{\mathrm{e}}}}{4\frac{dV}{d\ln c_{\mathrm{e}}}}. \tag{49}$$

Here F is the Faraday constant, c_{e0} is the bulk salt concentration, D_{e} is the diffusivity and $\frac{dV}{d\ln c_{\mathrm{e}}}$ is the concentration dependence of the derivative of the measured voltage (the diffusion potential) with respect to the logarithm of the concentration. Note that this method requires independent concentration cell and diffusion coefficient measurements to determine D_{e} and $\frac{dV}{d\ln c_{\mathrm{e}}}$, and so care must be taken to preclude the propagation of experimental errors. While valid for non-ideal electrolytes, this relationship is derived using concentrated solution theory, assuming a binary electrolyte with electrode reactions under anion-blocking conditions. Several groups have used the galvanostatic polarisation method to measure transport properties in non-aqueous LiB electrolytes [201, 206, 216, 233, 237]. Farkhondeh *et al* [234] have also fitted their four-electrode galvanostatic-pulse relaxation experiments with a transport model, to extract electrolyte transport properties.

5.2.2.3. Potentiostatic polarisation

The potentiostatic polarisation, or steady-state direct current, method was popularised by Bruce and Vincent [238] for transference measurements in polymer electrolytes. The property measured by this method is better described as a current fraction [239] or transport number, t_+ [204, 209, 225], since infinite dilution is assumed in the original derivation of equation (50)—implying that ionic species are non-interacting. It should be emphasised that the interpretation of parameters t_+ and t_+^0 is distinct. Analysis by Bergstrom *et al* [232] has shown that potentiostatic polarisation measurements with liquid electrolytes are highly susceptible to the instability of lithium metal electrode surfaces. As such, t_+ cannot be used to parameterise models that accurately predict ion flux through the electrolyte phase.

The original Bruce–Vincent method applied a small constant potential bias (10 mV) and compared the initial and steady-state currents, after subtracting interfacial resistance effects, to determine the transference number via:

$$t_+ = \frac{I_{\mathrm{ss}}(V - I_{\mathrm{i}}R_{\mathrm{i}})}{I_{\mathrm{i}}(V - I_{\mathrm{ss}}R_{\mathrm{ss}})}. \tag{50}$$

Here, I_i is the initial current measured when a bias voltage, V, is applied, and i_{ss} is the steady-state current density. R_i and R_{ss} are the interfacial resistances (measured with EIS) from the electrodes, before and after polarisation. Hou and Monroe [204] have demonstrated that the propensity to underpredict concentration polarisation due to t_+ may be corrected for by accounting for the partial molar volume of salt. Recently, Balsara and Newman [240] have rederived the relationship between the steady-state current and transference number from concentrated solution theory, injecting the dependence of the diffusion coefficient and thermodynamic factor for higher salt compositions. Comparisons between galvanostatic and potentiostatic polarisation methods for transference numbers have been provided by Zugmann *et al* [216] and Ehrl *et al* [233].

5.2.2.4. Hittorf method
The Hittorf method measures the change in moles of cations, compared to anions, across the cell electrolyte cavity, with the passage of a set amount of charge [220, 241]. This ratio is then directly related to the transference number. Hou and Monroe [204] designed a densitometric Hittorf cell with stopcocks, allowing the isolation of anodic and cathodic chambers after polarisation. Once gradients in the isolated chambers relax, the changes in density between chambers could be used to determine the concentration difference. The transference number is related to the concentration difference via:

$$t_+^0 = 1 + \frac{F V_{\text{chamber}} \Delta c_e}{Q(1 - \overline{V}_e c_e)},$$

(51)

where V_{chamber} is the volume of the cell chamber where ion accumulation or depletion occurs, Δc_e is the final change in concentration between the neutral chamber and cathodic or anodic chambers, Q is the charge passed and $\overline{V}_e$ is the partial molar volume of salt attained from the density-molarity correlation. The overall change in composition from the Hittorf method may also by tracked conductometrically and potentiometrically [205].

5.2.3. Concentration cells
Concentration cells place two electrolytes with similar molecular species in chemical contact, to measure the liquid-junction potential that arises between them. This liquid-junction potential owes to the difference in chemical potential incurred by the different salt concentrations across the cell. When the OCV difference is measured with reversible lithium metal electrodes across the lithium-ion electrolyte concentration cell, the liquid-junction potential, ϕ_e, is related to the thermodynamic factor, $1 + \partial \ln f_\pm / \partial \ln c_e$, and transference, t_+^0, via the change in voltage with respect to c_e [195]:

$$\frac{\partial \phi_e}{\partial \ln c_e} = \frac{2RT}{F} \left(1 + \frac{\partial \ln f_\pm}{\partial \ln c_e} \right) \left(1 - t_+^0 \right).$$

(52)

The above equation can be derived by taking equation (4) at open-circuit (zero current) conditions.

Diffusion is controlled by placing both electrolytes in contact through a porous separator or frit with low porosity. By varying the reference and test concentrations on either side of the cell, the combination of the thermodynamic factor and the transference number that appears in equation (52) can be extracted. The thermodynamic factor for lithium-ion electrolytes is then isolated by an independent measurement of transference number via polarisation–relaxation experiments [201, 204–206, 209, 221, 225, 237]. Concentration-cell experiments inherently average the transference number across the concentration profile through the frit. The difference in test and reference concentrations should therefore be minimised, to prevent convolution of concomitant changes in transference and thermodynamic factors [209].

5.2.4. Spectroscopic techniques
Spectroscopic techniques, such as NMR spectroscopy, have been used to characterise electrolyte transport properties, largely from two directions. The first is using spectroscopy to extract entire lithium-ion concentration profiles. Often this is done with *in situ* magnetic resonance imaging (MRI). Similar polarisation-relaxation experiments are performed, but MRI is used in place of voltammetric or densitometric indicators of concentration. These profiles are used to validate [242] or inversely fit relevant transport properties [223, 231, 243]. Raman spectroscopy and x-ray scattering has also been used to measure salt concentration profiles [224, 239]. Transport parameters obtained from inverse fitting are therefore highly dependent on the formulation of the models used to fit composition gradients.

Secondly, pulse-field gradient (PFG) NMR can be used to measure self-diffusion coefficients of nuclei in electrolytes, which relates to their equilibrium Brownian motion. By using radio-frequency pulses along with magnetic field gradients, spatial information on cation, anion, or solvent nuclei can then be encoded.

Because PFG-NMR does not distinguish between charged and neutral species, assumptions need to be made to translate self-diffusion coefficients into transport properties of charge carriers [244]. Srinivasan's research group connected PFG-NMR results with Onsager-Stefan-Maxwell concentrated solution theory, by calculating binary interaction parameters using a Darken relation between individual diffusivities [211, 245]. Discrepancies in PFG-NMR results may stem from the lack of electric field and chemical potential driving forces, which are present during battery operation. An emerging technique involves applying a large electric field to PFG-NMR known as electrophoretic NMR. The measured instantaneous velocity between species is then used to interpret transport properties [217, 246, 247].

5.2.5. Densitometry

The electrolyte density can easily be attained by comparing the mass and volume of a particular solution. It is commonly measured with commercial densitometers, that operate based on the oscillating U-tube principle [201, 204, 209, 223, 224]. By vibrating a container filled with solution, the frequency is then linked to the mass per unit volume.

Partial molar volumes, as discussed in section 5.1.5, give the change in volume of a solution per mole of solvent, $\overline{V}_0$, or salt, $\overline{V}_e$, added. The partial molar volumes are directly related to the way density, ρ, changes as a function of salt concentration, c_e, [195]:

$$\overline{V}_e = \frac{M_e - \dfrac{d\rho}{dc_e}}{\rho - c_e \dfrac{d\rho}{dc_e}}, \quad \overline{V}_0 = \frac{M_0}{\rho - c_e \dfrac{d\rho}{dc_e}}, \tag{53}$$

where M_0, M_e are the respective molar masses of solvent and salt.

6. Parameter database

As part of this review, we provide a free and open database of battery, and DFN model, parameters called LiionDB, available at www.liiondb.com [20]. Open battery data repositories like this will continue to aid researchers across the energy storage spectrum. For example, the Battery Genome and Battery Archive initiatives both provide frameworks for open-source data sharing [248, 249]. Reis *et al* [250] have also summarised public sources of battery cycling aging data for different chemistries and operating conditions. Other tools, such as the Battery Explorer by the Materials Project, provide a database of material properties that can accelerate compound discoveries [251]. Text-mining approaches have been applied to parse a large quantity of published literature, to extract relevant material properties [252, 253].
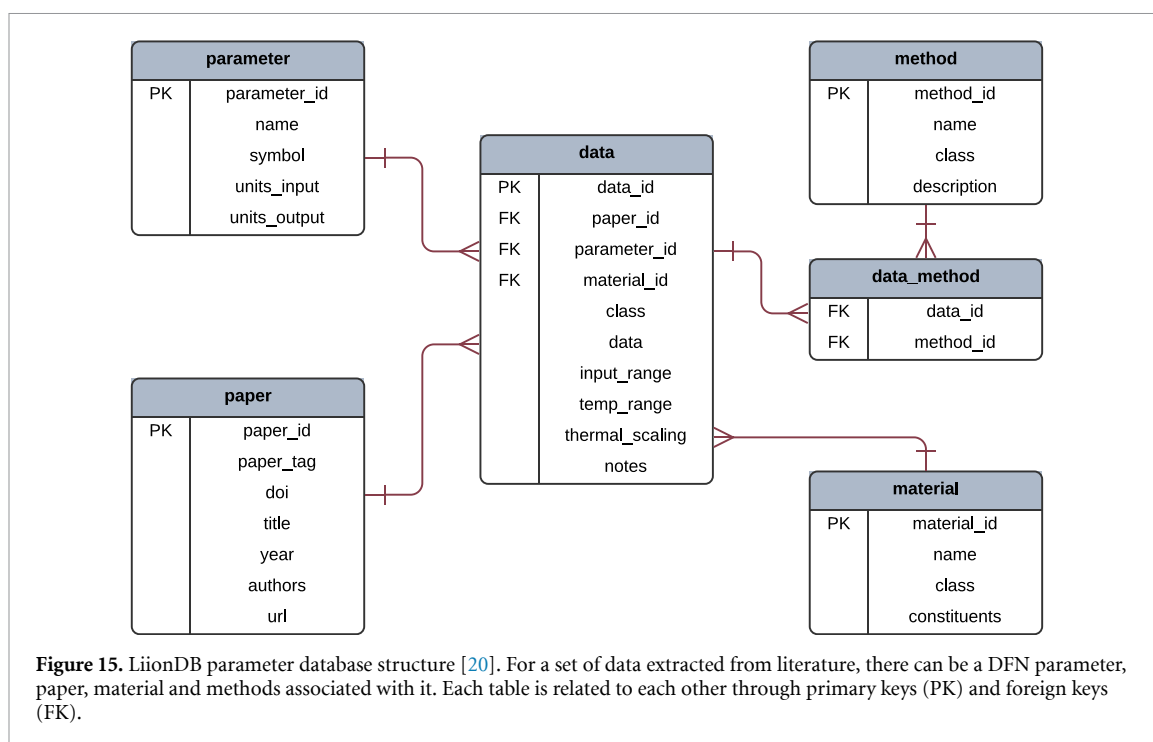
The complexity in DFN property relations precluded auto-parsing of literature parameters via data-driven techniques in this review. Hence, parameters were abstracted individually by reproducing values or correlations where provided, or extracted manually from published plots.

The database parameters reported alongside this manuscript were limited to literature sources for lithium-ion cell chemistries, with a focus on relevance to DFN-based battery models. They are presented in a searchable PostgreSQL format, along with a GUI web application (at www.liiondb.com) [20]. A schematic of the database structure is depicted in figure 15. At the time of publishing, there are 1000+ parameter data sets in scalar and functional forms across the materials and papers included. Each data set is also associated with the methods broadly employed during its direct or inverse measurement. The applicable composition range, temperature and thermal scaling methods are also stated, where available. Material sub-components have also been individually included, to maintain search flexibility.

The authors caution against parameterising battery models without regard for the contextual origin of chosen properties. Best practice guidelines for battery modelling should be followed [254]. This database acts as a directory for a range of parameter values reported in the literature, allowing modellers access to the context of how the physical parameters were measured. As covered in sections 3.2, 4.2 and 5.2, many properties are method-specific and compatibility with model formulation should be confirmed, to ensure physical consistency.

6.1. Contributing to the database

We encourage the community to contribute towards LiionDB. On the website www.liiondb.com [20], we have provided information on how authors can submit their data for inclusion. This will not only serve the community in general, by making the database more comprehensive, but also offers contributors better visibility for their work, leading to more citations and interaction with other research groups around the globe.

Figure 15. LiionDB parameter database structure [20]. For a set of data extracted from literature, there can be a DFN parameter, paper, material and methods associated with it. Each table is related to each other through primary keys (PK) and foreign keys (FK).

7. Discussion and conclusions

The DFN modelling framework has become a ubiquitous tool for carrying out cell-scale simulations of LiBs. Despite its widespread use, challenges remain around how to fully and accurately determine the scalar and functional parameters that are required for its use. Whilst a great deal of characterisation has been reported in the literature, there was no central repository where independent measurements are collated and can be compared. The database that accompanies this review (available at www.liiondb.com) fills this need and we hope that it will serve the battery modelling community, by becoming the main resource for finding DFN model parameter values.

The second purpose of this review is to inform modellers and experimentalists alike about some of the often unstated assumptions implicit in the methods used to infer parameter values from raw experimental data. The aim here is to prevent researchers from using parameter values which were extracted under assumptions inconsistent with the operating conditions in which they aim to use their model. This is critical, to ensure that models have genuinely robust predictive power. For many parameter values, the consistency of assumptions is clear. For other parameter values, for example, the solid-state diffusivity as inferred by EIS, there are typically numerous (and more subtle) assumptions at play, e.g. whether insertion materials are treated as spherical or planar with semi-infinite geometry. The parameterisation challenge is further complicated by the issue of identifiability: a nondimensionalisation of the equations can be carried out to reveal which parameters can be learned from a given experiment and which parameters are required to parameterise a model. We hope that this review serves to make these assumptions clear, thereby empowering researchers to make informed choices about which parameter values are most appropriate for their particular situation.

A compounding issue that applies to many parameters is the propagation of errors in the parameterisation process. Consider again the solid-state diffusion coefficient. The model used to convert the raw experimental data to a diffusion coefficient requires the input of geometrical properties, e.g. the electrochemically active surface area of the electrode particles. This quantity is almost always not known exactly and instead has to be estimated by another experimental procedure. Thus, we must be mindful of how these errors can potentially propagate.

Although this review has focused primarily on the DFN model, there are many applications in which reduced models give sufficient predictive power. For example, a cell phone battery discharging at a modest C-rate is well-described by a so-called 'single particle model'. In such cases, it is prudent to utilise these reduced models, not only in the interests of computational efficiency, but also because they typically contain fewer parameters and are therefore simpler to parameterise.

Despite all these difficulties, the DFN framework is an extremely powerful tool and has been used to great effect in helping to accelerate LiB development.

Data availability statement

All data that support the findings of this study are included within the article (and any supplementary files).

Acknowledgments

ORCID iDs

A A Wang ⓘ https://orcid.org/0000-0003-1864-5213
S E J O'Kane ⓘ https://orcid.org/0000-0003-3141-1657
F Brosa Planella ⓘ https://orcid.org/0000-0001-6363-2812
J Le Houx ⓘ https://orcid.org/0000-0002-1576-0673
K O'Regan ⓘ https://orcid.org/0000-0002-5266-594X
J Edge ⓘ https://orcid.org/0000-0003-4643-2426
C W Monroe ⓘ https://orcid.org/0000-0002-9894-5023
S J Cooper ⓘ https://orcid.org/0000-0003-4055-6903
D A Howey ⓘ https://orcid.org/0000-0002-0620-3955
E Kendrick ⓘ https://orcid.org/0000-0002-4219-964X
J M Foster ⓘ https://orcid.org/0000-0002-6120-5734

References

[1] Ue M, Sakaushi K and Uosaki K 2020 Basic knowledge in battery research bridging the gap between academia and industry *Mater. Horiz.* **7** 1937–54
[2] Newman J 1961 A model for the analysis of the behavior of porous electrodes *NOLC Project (and Master's Thesis)*
[3] Newman J S and Tobias C W 1962 Theoretical analysis of current distribution in porous electrodes *J. Electrochem. Soc.* **109** 1183–91
[4] Newman J and Tiedemann W 1975 Porous-electrode theory with battery applications *AIChE J.* **21** 25–41
[5] Doyle M, Fuller T F and Newman J 1993 Modeling of galvanostatic charge and discharge of the lithium/polymer/insertion cell *J. Electrochem. Soc.* **140** 1526
[6] Fuller T F, Doyle M and Newman J 1994 Simulation and optimization of the dual lithium ion insertion cell *J. Electrochem. Soc.* **141** 1
[7] Ma Y, Doyle M, Fuller T F, Doeff M M, De Jonghe L C and Newman J 1995 The measurement of a complete set of transport properties for a concentrated solid polymer electrolyte solution *J. Electrochem. Soc.* **142** 1859–68
[8] Doyle M and Newman J 1995 The use of mathematical modeling in the design of lithium/polymer battery systems *Electrochim. Acta* **40** 2191–6
[9] Doyle M, Newman J, Gozdz A S, Schmutz C N and Tarascon J-M 1996 Comparison of modeling predictions with experimental data from plastic lithium ion cells *J. Electrochem. Soc.* **143** 1890–903
[10] Thomas K E, Newman J and Darling R M 2002 Mathematical modeling of lithium batteries *Advances in Lithium-Ion Batteries* (Berlin: Springer) pp 345–92
[11] Richardson G, Denuault G and Please C P 2012 Multiscale modelling and analysis of lithium-ion battery charge and discharge *J. Eng. Math.* **72** 41–72
[12] Ciucci F and Lai W 2011 Derivation of micro/macro lithium battery models from homogenization *Transp. Porous Media* **88** 249–70
[13] Díaz J, Gómez-Castro D and Ramos A M 2018 On the well-posedness of a multiscale mathematical model for lithium-ion batteries *Adv. Nonlinear Anal.* **8** 1132–57
[14] Li G and Monroe C W 2020 Multiscale lithium-battery modeling from materials to cells *Annu. Rev. Chem. Biomol. Eng.* **11** 277–310
[15] Laue V, Röder F and Krewer U 2021 Practical identifiability of electrochemical P2D models for lithium-ion batteries *J. Appl. Electrochem.* **51** 1253–65
[16] Bizeray A M, Kim J-H, Duncan S R and Howey D A 2019 Identifiability and parameter estimation of the single particle lithium-ion battery model *IEEE Trans. Control Syst. Technol.* **27** 1862–77
[17] Ecker M, Tran T K D, Dechent P, Käbitz S, Warnecke A and Sauer D U 2015 Parameterization of a physico-chemical model of a lithium-ion battery *J. Electrochem. Soc.* **162** A1836–48
[18] Zülke A, Korotkin I, Foster J M, Nagarathinam M, Hoster H and Richardson G 2021 Parametrisation and use of a predictive DFN model for a high-energy NCA/Gr-SiOx battery *J. Electrochem. Soc.* **168** 120522
[19] Chen C-H, Brosa Planella F, O'Regan K, Gastol D, Widanage W D and Kendrick E 2020 Development of experimental techniques for parameterization of multi-scale lithium-ion battery models *J. Electrochem. Soc.* **167** 080534
[20] Wang A and Sulzer V 2021 ndrewwang/liiondb: first release of LiionDB

[21] Gerver R E and Meyers J P 2011 Three-dimensional modeling of electrochemical performance and heat generation of lithium-ion batteries in tabbed planar configurations *J. Electrochem. Soc.* **158** A835

[22] McCleary D A H, Meyers J P and Kim B 2013 Three-dimensional modeling of electrochemical performance and heat generation of spirally and prismatically wound lithium-ion batteries *J. Electrochem. Soc.* **160** A1931–43

[23] Tang M, Albertus P and Newman J 2009 Two-dimensional modeling of lithium deposition during cell charging *J. Electrochem. Soc.* **156** A390

[24] Rosser T E, Dickinson E J F, Raccichini R, Hunter K, Searle A D, Kavanagh C M, Curran P J, Hinds G, Park J and Wain A J 2021 Improved operando Raman cell configuration for commercially-sourced electrodes in alkali-ion batteries *J. Electrochem. Soc.* **168** 070541

[25] Marquis S G, Timms R, Sulzer V, Please C P and Jon Chapman S 2020 A suite of reduced-order models of a single-layer lithium-ion pouch cell *J. Electrochem. Soc.* **167** 140513

[26] Tranter T G, Timms R, Shearing P R and Brett D J L 2020 Communication–prediction of thermal issues for larger format 4680 cylindrical cells and their mitigation with enhanced current collection *J. Electrochem. Soc.* **167** 160544

[27] Alipour M, Ziebert C, Conte F V and Kizilel R 2020 A review on temperature-dependent electrochemical properties, aging and performance of lithium-ion cells *Batteries* **6** 35

[28] Richardson G and Korotkin I 2021 Heat generation and a conservation law for chemical energy in li-ion batteries *Electrochim. Acta* **392** 138909

[29] Kim S U, Albertus P, Cook D, Monroe C W and Christensen J 2014 Thermoelectrochemical simulations of performance and abuse in 50-Ah automotive cells *J. Power Sources* **268** 625–33

[30] Erhard S V *et al* 2017 Simulation and measurement of the current density distribution in lithium-ion batteries by a multi-tab cell approach *J. Electrochem. Soc.* **164** A6324

[31] Rieger B, Erhard S V, Kosch S, Venator M, Rheinfeld A and Jossen A 2016 Multi-dimensional modeling of the influence of cell design on temperature, displacement and stress inhomogeneity in large-format lithium-ion cells *J. Electrochem. Soc.* **163** A3099

[32] Fear C, Parmananda M, Kabra V, Carter R, Love C T and Mukherjee P P 2021 Mechanistic underpinnings of thermal gradient induced inhomogeneity in lithium plating *Energy Storage Mater.* **35** 500–11

[33] Ong I J and Newman J 1999 Double-layer capacitance in a dual lithium ion insertion cell *J. Electrochem. Soc.* **146** 4360–5

[34] Legrand N, Raël S, Knosp B, Hinaje M, Desprez P and Lapicque F 2014 Including double-layer capacitance in lithium-ion battery mathematical models *J. Power Sources* **251** 370–8

[35] Kirk T L, Evans J, Please C P and Chapman S J 2020 Modelling electrode heterogeneity in lithium-ion batteries: unimodal and bimodal particle-size distributions (arXiv:2006.12208 [physics.app-ph])

[36] Krachkovskiy S A, Foster J M, David Bazak J, Balcom B J and Goward G R 2018 Operando mapping of Li concentration profiles and phase transformations in graphite electrodes by magnetic resonance imaging and nuclear magnetic resonance spectroscopy *J. Phys. Chem.* C **122** 21784–91

[37] Zülke A, Korotkin I, Foster J M, Nagarathinam M, Hoster H and Richardson G 2021 Parametrisation and use of a predictive DFN model for a high-energy NCA/Gr-SiOx battery *J. Electrochem. Soc.* **168** 120522

[38] Dai Y, Cai L and White R E 2013 Capacity fade model for spinel $LiMn_2O_4$ electrode *J. Electrochem. Soc.* **160** A182–90

[39] Chen L-C and Ho. K-C 2002 Nonlinear diffusion behavior for the Prussian blue electrode. II. Interpretation of variable diffusivity during the insertion/extraction processes *J. Electrochem. Soc.* **149** E40

[40] Zhang X, Shyy W and Sastry A M 2007 Numerical simulation of intercalation-induced stress in Li-ion battery electrode particles *J. Electrochem. Soc.* **154** A910

[41] Thornton K, Ågren J and Voorhees P W 2003 Modelling the evolution of phase boundaries in solids at the meso- and nano-scales *Acta Mater.* **51** 5675–710

[42] Franco A A 2013 Multiscale modelling and numerical simulation of rechargeable lithium ion batteries: concepts, methods and challenges *RSC Adv.* **3** 13027

[43] Zhang Q and White R E 2007 Moving boundary model for the discharge of a $LiCoO_2$ electrode *J. Electrochem. Soc.* **154** A587

[44] Srinivasan V and Newman J 2004 Design and optimization of a natural graphite/iron phosphate lithium-ion cell *J. Electrochem. Soc.* **151** A1530

[45] Bazant M Z 2013 Theory of chemical kinetics and charge transfer based on nonequilibrium thermodynamics *Acc. Chem. Res.* **46** 1144–60

[46] Newman J 1995 Optimization of porosity and thickness of a battery electrode by means of a reaction-zone model *J. Electrochem. Soc.* **142** 97–101

[47] Karthikeyan D K, Sikha G and White R E 2008 Thermodynamic model development for lithium intercalation electrodes *J. Power Sources* **185** 1398–407

[48] Costard J, Joos J, Schmidt A and Ivers-Tiffée E Charge transfer parameters of $Ni_xMn_yCo_{1-x-y}$ cathodes evaluated by a transmission line modeling approach *Energy Technol.* 2000866

[49] Marquis S G, Sulzer V, Timms R, Please C P and Chapman S J 2019 An asymptotic derivation of a single particle model with electrolyte *J. Electrochem. Soc.* **166** A3693

[50] Li Y, Vilathgamuwa M, Farrell T, Choi S S, Tran N T and Teague J 2019 A physics-based distributed-parameter equivalent circuit model for lithium-ion batteries *Electrochim. Acta* **299** 451–69

[51] Castle M, Richardson G and Foster J M 2021 Understanding rapid charge and discharge in nano-structured lithium iron phosphate cathodes *Eur. J. Appl. Math.* **33** 1–41

[52] Lu X *et al* 2020 3D microstructure design of lithium-ion battery electrodes assisted by x-ray nano-computed tomography and modelling *Nat. Commun.* **11** 1–13

[53] Louli A J, Li J, Trussler S, Fell C R and Dahn J R 2017 Volume, pressure and thickness evolution of Li-ion pouch cells with silicon-composite negative electrodes *J. Electrochem. Soc.* **164** A2689–96

[54] Foster J M, Huang X, Jiang M, Chapman S J, Protas B and Richardson G 2017 Causes of binder damage in porous battery electrodes and strategies to prevent it *J. Power Sources* **350** 140–51

[55] McDowell M T, Xia S and Zhu T 2016 The mechanics of large-volume-change transformations in high-capacity battery materials *Extreme Mech. Lett.* **9** 480–94

[56] Zhang X, Chumakov S, Li X, Klinsmann M, Kim S U, Linder C and Christensen J 2020 An electro-chemo-thermo-mechanical coupled three-dimensional computational framework for lithium-ion batteries *J. Electrochem. Soc.* **167** 160542

[57] Deng Z, Huang Z, Shen Y, Huang Y, Ding H, Luscombe A, Johnson M, Harlow J E, Gauthier R and Dahn J R 2020 Ultrasonic scanning to observe wetting and "Unwetting" in Li-ion pouch cells *Joule* **4** 2017–29

[58] Neidhardt J P, Fronczek D N, Jahnke T, Danner T, Horstmann B and Bessler W G 2012 A flexible framework for modeling multiple solid, liquid and gaseous phases in batteries and fuel cells *J. Electrochem. Soc.* **159** A1528–42

[59] Yang X-G, Leng Y, Zhang G, Ge S and Wang C-Y 2017 Modeling of lithium plating induced aging of lithium-ion batteries: transition from linear to nonlinear aging *J. Power Sources* **360** 28–40

[60] Cui S *et al* 2016 Optimized temperature effect of Li-ion diffusion with layer distance in $Li(Ni_xMn_yCo_z)O_2$ cathode materials for high performance Li-ion battery *Adv. Energy Mater.* **6** 1501309

[61] Ko J Y, Varini M, Klett M, Ekström H and Lindbergh G 2019 Porous electrode model with particle stress effects for $Li(Ni_{1/3}Co_{1/3}Mn_{1/3})O_2$ electrode *J. Electrochem. Soc.* **166** A2939–49

[62] Hosseinzadeh E, Marco J and Jennings P 2018 The impact of multi-layered porosity distribution on the performance of a lithium ion battery *Appl. Math. Modelling* **61** 107–23

[63] Zhao L, Bennett J C and Obrovac M N 2018 Hexagonal platelet graphite and its application in Li-ion batteries *Carbon* **134** 507–18

[64] Persson K, Sethuraman V A, Hardwick L J, Hinuma Y, Meng Y S, van der Ven A, Srinivasan V, Kostecki R and Ceder G 2010 Lithium diffusion in graphitic carbon *J. Phys. Chem. Lett.* **1** 1176–80

[65] Landesfeind J, Hattendorff J, Ehrl A, Wall W A and Gasteiger H A 2016 Tortuosity determination of battery electrodes and separators by impedance spectroscopy *J. Electrochem. Soc.* **163** A1373–87

[66] Usseglio-Viretta F L E *et al* 2018 Resolving the discrepancy in tortuosity factor estimation for Li-ion battery electrodes through micro-macro modeling and experiment *J. Electrochem. Soc.* **165** A3403

[67] Tjaden B, Cooper S J, Brett D J, Kramer D and Shearing P R 2016 On the origin and application of the Bruggeman correlation for analysing transport phenomena in electrochemical systems *Curr. Opin. Chem. Eng.* **12** 44–51

[68] Chung D-W, Ebner M, Ely D R, Wood V and Edwin García R E 2013 Validity of the Bruggeman relation for porous electrodes *Modelling Simul. Mater. Sci. Eng.* **21** 074009

[69] Nguyen T-T, Demortière A, Fleutot B, Delobel B, Delacourt C and Cooper S J 2020 The electrode tortuosity factor: why the conventional tortuosity factor is not well suited for quantifying transport in porous Li-ion battery electrodes and what to use instead *npj Comput. Mater.* **6** 1–12

[70] Epstein N 1989 On tortuosity and the tortuosity factor in flow and diffusion through porous media *Chem. Eng. Sci.* **44** 777–9

[71] Peterson S W and Wheeler D R 2014 Direct measurements of effective electronic transport in porous Li-ion electrodes *J. Electrochem. Soc.* **161** A2175–81

[72] Amin R and Chiang Y-M 2016 Characterization of electronic and ionic transport in $Li_{1-x}Ni_{0.33}Mn_{0.33}Co_{0.33}O_2$ (NMC_{333}) and $Li_{1-x}Ni_{0.50}Mn_{0.20}Co_{0.30}O_2$ (NMC_{523}) as a function of Li content *J. Electrochem. Soc.* **163** A1512–7

[73] Qi X, Blizanac B, DuPasquier A, Oljaca M, Li J and Winter M 2013 Understanding the influence of conductive carbon additives surface area on the rate performance of $LiFePO_4$ cathodes for lithium ion batteries *Carbon* **64** 334–40

[74] Goldstein J I, Newbury D E, Michael J R, Ritchie N W M, Scott J H J and Joy D C 2017 *Scanning Electron Microscopy and X-ray Microanalysis* (Berlin: Springer)

[75] Ostadi H, Rama P, Liu Y, Chen R, Zhang X X and Jiang K 2010 3D reconstruction of a gas diffusion layer and a microporous layer *J. Membr. Sci.* **351** 69–74

[76] Ziegler C, Thiele S and Zengerle R 2011 Direct three-dimensional reconstruction of a nanoporous catalyst layer for a polymer electrolyte fuel cell *J. Power Sources* **196** 2094–7

[77] Stephenson D E, Walker B C, Skelton C B, Gorzkowski E P, Rowenhorst D J and Wheeler D R 2011 Modeling 3D microstructure and ion transport in porous Li-ion battery electrodes *J. Electrochem. Soc.* **158** A781

[78] Le Houx J, Osenberg M, Neumann M, Binder J R, Schmidt V, Manke I, Carraro T and Kramer D 2020 Effect of tomography resolution on calculation of microstructural properties for lithium ion porous electrodes *ECS Trans.* **97** 255

[79] Finegan D P, Cooper S J, Tjaden B, Taiwo O O, Gelb J, Hinds G, Brett D J L and Shearing P R 2016 Characterising the structural properties of polymer separators for lithium-ion batteries in 3D using phase contrast x-ray microscopy *J. Power Sources* **333** 184–92

[80] Wargo E A, Kotaka T, Tabuchi Y and Kumbur E C 2013 Comparison of focused ion beam versus nano-scale x-ray computed tomography for resolving 3-D microstructures of porous fuel cell materials *J. Power Sources* **241** 608–18

[81] Le Houx J and Kramer D 2021 X-ray tomography for lithium ion battery electrode characterisation—a review *Energy Rep.* **7** 9–14

[82] Ebner M, Chung D-W, García R E and Wood V 2014 Tortuosity anisotropy in lithium-ion battery electrodes *Adv. Energy Mater.* **4** 1301278

[83] Kehrwald D, Shearing P R, Brandon N P, Sinha P K and Harris S J 2011 Local tortuosity inhomogeneities in a lithium battery composite electrode *J. Electrochem. Soc.* **158** A1393

[84] Ebner M, Marone F, Stampanoni M and Wood V 2013 Visualization and quantification of electrochemical and mechanical degradation in Li ion batteries *Science* **342** 716–20

[85] Le Houx J and Kramer D 2020 Physics based modelling of porous lithium ion battery electrodes—a review *Energy Rep.* **6** 1–9

[86] Cooper S J, Bertei A, Shearing P R, Kilner J A and Brandon N P 2016 TauFactor: an open-source application for calculating tortuosity factors from tomographic data *SoftwareX* **5** 203–10

[87] Gostick J *et al* 2016 OpenPNM: a pore network modeling package *Comput. Sci. Eng.* **18** 60–74

[88] Trembacki B L, Noble D R, Brunini V E, Ferraro M E and Roberts S A 2017 Mesoscale effective property simulations incorporating conductive binder *J. Electrochem. Soc.* **164** E3613–26

[89] Chouchane M, Rucci A, Lombardo T, Ngandjong A C and Franco A A 2019 Lithium ion battery electrodes predicted from manufacturing simulations: assessing the impact of the carbon-binder spatial location on the electrochemical performance *J. Power Sources* **444** 227285

[90] Orazem M E and Tribollet B 2008 *Electrochemical Impedance Spectroscopy* (Berlin: Wiley)

[91] Li S E, Wang B, Peng H and Hu X 2014 An electrochemistry-based impedance model for lithium-ion batteries *J. Power Sources* **258** 9–18

[92] Wang Q-K, He Y-J, Shen J-N, Hu X-S and Ma Z-F 2018 State of charge-dependent polynomial equivalent circuit modeling for electrochemical impedance spectroscopy of lithium-ion batteries *IEEE Trans. Power Electron.* **33** 8449–60

[93] Doyle M, Meyers J P and Newman J 2000 Computer simulations of the impedance response of lithium rechargeable batteries *J. Electrochem. Soc.* **147** 99

[94] Ebner M, Geldmacher F, Marone F, Stampanoni M and Wood V 2013 X-ray tomography of porous, transition metal oxide based lithium ion battery electrodes *Adv. Energy Mater.* **3** 845–50

[95] Drezen T, Kwon N-H, Bowen P, Teerlinck I, Isono M and Exnar I 2007 Effect of particle size on $LiMnPO_4$ cathodes *J. Power Sources* **174** 949–53

[96] Eshel G, Levy G J, Mingelgrin U and Singer M J 2004 Critical evaluation of the use of laser diffraction for particle-size distribution analysis *Soil Sci. Soc. Am. J.* **68** 736–43

[97] Giesche H 2006 Mercury porosimetry: a general (practical) overview *Part. Part. Syst. Charact.* **23** 9–19

[98] Sheng Y, Fell C R, Son Y K, Metz B M, Jiang J and Church B C 2014 Effect of calendering on electrode wettability in lithium-ion batteries *Frontiers Energy Res.* **2** 56

[99] Schmalstieg J, Rahe C, Ecker M and Sauer D U 2018 Full cell parameterization of a high-power lithium-ion battery for a physico-chemical model: Part I. Physical and electrochemical parameters *J. Electrochem. Soc.* **165** A3799–810

[100] Mayer R P and Stowe R A 1965 Mercury porosimetry–breakthrough pressure for penetration between packed spheres *J. Colloid Sci.* **20** 893–911

[101] Sinha P, Datar A, Jeong C, Deng X, Chung Y G and Lin L-C 2019 Surface area determination of porous materials using the Brunauer-Emmett-Teller (BET) method: limitations and improvements *J. Phys. Chem.* C **123** 20195–209

[102] Cho J and Park B 2001 Preparation and electrochemical/thermal properties of $LiNi_{0.74}Co_{0.26}O_2$ cathode material *J. Power Sources* **92** 35–39

[103] Huang G, Xu S, Lu S, Li L and Sun H 2014 Micro-/nanostructured Co_3O_4 anode with enhanced rate capability for lithium-ion batteries *ACS Appl. Mater. Interfaces* **6** 7236–43

[104] Lim S, Yoon C S and Cho J 2008 Synthesis of nanowire and hollow $LiFePO_4$ cathodes for high-performance lithium batteries *Chem. Mater.* **20** 4560–4

[105] Winter M, Novák P and Monnier A 1998 Graphites for lithium-ion cells: the correlation of the first-cycle charge loss with the Brunauer-Emmett-Teller surface area *J. Electrochem. Soc.* **145** 428–36

[106] Birkl C R, McTurk E, Roberts M R, Bruce P G and Howey D A 2015 A parametric open circuit voltage model for lithium ion batteries *J. Electrochem. Soc.* **162** A2271

[107] Guggenheim E A 1929 The conceptions of electrical potential difference between two phases and the individual activities of ions *J. Phys. Chem.* **33** 842–9

[108] Reniers J M, Mulder G and Howey D A 2019 Review and performance comparison of mechanical-chemical degradation models for lithium-ion batteries *J. Electrochem. Soc.* **166** A3189–200

[109] Dees D, Gunen E, Abraham D, Jansen A and Prakash J 2008 Electrochemical modeling of lithium-ion positive electrodes during hybrid pulse power characterization tests *J. Electrochem. Soc.* **155** A603

[110] Zhang Q, Guo Q and White R E 2006 A new kinetic equation for intercalation electrodes *J. Electrochem. Soc.* **153** A301

[111] Lu D, Trimboli M S, Fan G, Zhang R and Plett G L 2021 Implementation of a physics-based model for half-cell open-circuit potential and full-cell open-circuit voltage estimates: part I. Processing half-cell data *J. Electrochem. Soc.* **168** 070532

[112] Lu D, Trimboli M S, Fan G, Zhang R and Plett G L 2021 Implementation of a physics-based model for half-cell open-circuit potential and full-cell open-circuit voltage estimates: part II. Processing full-cell data *J. Electrochem. Soc.* **168** 070533

[113] Farkhondeh M, Safari M, Pritzker M, Fowler M, Han T, Wang J and Delacourt C 2014 Full-range simulation of a commercial $LiFePO_4$ electrode accounting for bulk and surface effects: a comparative analysis *J. Electrochem. Soc.* **161** A201–12

[114] Verma A, Smith K, Santhanagopalan S, Abraham D, Yao K P and Mukherjee P P 2017 Galvanostatic intermittent titration and performance based analysis of $LiNi_{0.5}Co_{0.2}Mn_{0.3}O_2$ cathode *J. Electrochem. Soc.* **164** A3380–92

[115] Zhao S, Duncan S R and Howey D A 2017 Observability analysis and state estimation of lithium-ion batteries in the presence of sensor biases *IEEE Trans. Control Syst. Technol.* **25** 326–33

[116] Verbrugge M, Baker D, Koch B, Xiao X and Gu. W 2017 Thermodynamic model for substitutional materials: application to lithiated graphite, spinel manganese oxide, iron phosphate and layered nickel-manganese-cobalt oxide *J. Electrochem. Soc.* **164** E3243

[117] Assat G, Glazier S L, Delacourt C and Tarascon J-M 2019 Probing the thermal effects of voltage hysteresis in anionic redox-based lithium-rich cathodes using isothermal calorimetry *Nat. Energy* **4** 647–56

[118] Plett G L 2015 *Battery Management Systems, Volume I: Battery Modeling* (Norwood, MA: Artech House)

[119] Ghosh A, Foster J M, Offer G and Marinescu M 2021 A shrinking-core model for the degradation of high-nickel cathodes (NMC811) in Li-ion batteries: passivation layer growth and oxygen evolution *J. Electrochem. Soc.* **168** 020509

[120] Birkl C R, Roberts M R, McTurk E, Bruce P G and Howey D A 2017 Degradation diagnostics for lithium ion cells *J. Power Sources* **341** 373–86

[121] Wu S-L, Zhang W, Song X, Shukla A K, Liu G, Battaglia V and Srinivasan V 2012 High rate capability of $Li(Ni_{1/3}Mn_{1/3}Co_{1/3})O_2$ electrode for Li-ion batteries *J. Electrochem. Soc.* **159** A438–44

[122] Danner T, Singh M, Hein S, Kaiser J, Hahn H and Latz A 2016 Thick electrodes for Li-ion batteries: a model based analysis *J. Power Sources* **334** 191–201

[123] Bai P and Bazant M Z 2014 Charge transfer kinetics at the solid-solid interface in porous electrodes *Nat. Commun.* **5** 3538

[124] Smith R B and Bazant M Z 2017 Multiphase porous electrode theory *J. Electrochem. Soc.* **164** E3291–310

[125] Dickinson E J F and Wain A J 2020 The Butler-Volmer equation in electrochemical theory: origins, value and practical application *J. Electroanal. Chem.* **872** 114145

[126] Albertus P, Christensen J and Newman J 2009 Experiments on and modeling of positive electrodes with multiple active materials for lithium-ion batteries *J. Electrochem. Soc.* **156** A606

[127] Sripad S, Korff D, DeCaluwe S C and Viswanathan V 2020 Kinetics of lithium electrodeposition and stripping *J. Chem. Phys.* **153** 194701

[128] Kurchin R and Viswanathan V 2020 Marcus-Hush-Chidsey kinetics at electrode-electrolyte interfaces *J. Chem. Phys.* **153** 134706

[129] O'Kane S E J, Campbell I D, Marzook M W J, Offer G J and Marinescu M 2020 Physical origin of the differential voltage minimum associated with lithium plating in li-ion batteries *J. Electrochem. Soc.* **167** 090540

[130] Ernst S, Heins T P, Schlüter N and Schröder U 2019 Capturing the current-overpotential nonlinearity of lithium-ion batteries by nonlinear electrochemical impedance spectroscopy (NLEIS) in charge and discharge direction *Frontiers Energy Res.* **7**

[131] Li Y and Qi Y 2019 Energy landscape of the charge transfer reaction at the complex Li/SEI/electrolyte interface *Energy Environ. Sci.* **12** 1286–95

[132] Yang X-G, Liu T, Gao Y, Ge S, Leng Y, Wang D and Wang C-Y 2019 Asymmetric temperature modulation for extreme fast charging of lithium-ion batteries *Joule* **3** 3002–19

[133] Park S, Kato D, Gima Z, Klein R and Moura S 2018 Optimal experimental design for parameterization of an electrochemical lithium-ion battery model *J. Electrochem. Soc.* **165** A1309–23

[134] Dufour N 2019 Physics-based modeling of graphite electrodes inside lithium-ion battery: study of lithiation heterogeneities and aging mechanisms *PhD Thesis* Communauté Université Grenoble Alpes

[135] Li W, Cao D, Jöst D, Ringbeck F, Kuipers M, Frie F and Sauer D U 2020 Parameter sensitivity analysis of electrochemical model-based battery management systems for lithium-ion batteries *Appl. Energy* **269** 115104

[136] Levi M D and Aurbach D 1997 Diffusion coefficients of lithium ions during intercalation into graphite derived from the simultaneous measurements and modeling of electrochemical impedance and potentiostatic intermittent titration characteristics of thin graphite electrodes *J. Phys. Chem.* B **101** 4641–7

[137] Van der Ven A, Bhattacharya J and Belak A A 2013 Understanding Li diffusion in Li-intercalation compounds *Acc. Chem. Res.* **46** 1216–25

[138] Baker D R and Verbrugge M W 2012 Intercalate diffusion in multiphase electrode materials and application to lithiated graphite *J. Electrochem. Soc.* **159** A1341–50

[139] Cabañero M A, Boaretto N, Röder M, Müller J, Kallo J and Latz A 2018 Direct determination of diffusion coefficients in commercial Li-ion batteries *J. Electrochem. Soc.* **165** A847–55

[140] Han S, Park J, Lu W and Sastry A M 2013 Numerical study of grain boundary effect on Li+ effective diffusivity and intercalation-induced stresses in Li-ion battery active materials *J. Power Sources* **240** 155–67

[141] Yang S, Yan B, Lu Li and Zeng K 2016 Grain boundary effects on Li-ion diffusion in a $Li_{1.2}Co_{0.13}Ni_{0.13}Mn_{0.54}O_2$ thin film cathode studied by scanning probe microscopy techniques *RSC Adv.* **6** 94000–9

[142] Trevisanello E, Ruess R, Conforto G, Richter F H and Janek J 2021 Polycrystalline and single crystalline NCM cathode materials—quantifying particle cracking, active surface area and lithium diffusion *Adv. Energy Mater.* **11** 2003400

[143] Cahn J W and Hilliard J E 1958 Free energy of a nonuniform system. i. interfacial free energy *J. Chem. Phys.* **28** 258–67

[144] Novick-Cohen A and Segel L A 1984 Nonlinear aspects of the Cahn-Hilliard equation *Physica* D **10** 277–98

[145] Morales Escalante J, Ko W, Foster J M, Krachkovskiy S, Goward G and Protas B 2020 Discerning models of phase transformations in porous graphite electrodes: insights from inverse modelling based on MRI measurements *Electrochim. Acta* **349** 136290

[146] Miccoli I, Edler F, Pfnür H and Tegenkamp C 2015 The 100th anniversary of the four-point probe technique: the role of probe geometries in isotropic and anisotropic systems *J. Phys.: Condens. Matter.* **27** 223201

[147] Mandal S, Amarilla J M, Ibáñez J and Rojo J M 2001 The role of carbon black in $LiMn_2O_4$-based composites as cathodes for rechargeable lithium batteries *J. Electrochem. Soc.* **148** A24

[148] Chen Y-H, Wang C-W, Liu G, Song X-Y, Battaglia V S and Sastry A M 2007 Selection of conductive additives in Li-ion battery cathodes *J. Electrochem. Soc.* **154** A978

[149] Smits F M 1958 Measurement of sheet resistivities with the four-point probe *Bell Syst. Tech. J.* **37** 711–8

[150] Illig J, Ender M, Chrobak T, Schmidt J P, Klotz D and Ivers-Tiffée E 2012 Separation of charge transfer and contact resistance in $LiFePO_4$-cathodes by impedance modeling *J. Electrochem. Soc.* **159** A952–60

[151] Tian R, Park S-H, King P J, Cunningham G, Coelho J, Nicolosi V and Coleman J N 2019 Quantifying the factors limiting rate performance in battery electrodes *Nat. Commun.* **10** 264–70

[152] Kondo H, Sawada H, Okuda C and Sasaki T 2019 Influence of the active material on the electronic conductivity of the positive electrode in lithium-ion batteries *J. Electrochem. Soc.* **166** A1285–90

[153] Lanterman B J, Riet A A, Gates N S, Flygare J D, Cutler A D, Vogel J E, Wheeler D R and Mazzeo B A 2015 Micro-four-line probe to measure electronic conductivity and contact resistance of thin-film battery electrodes *J. Electrochem. Soc.* **162** A2145–51

[154] Ender M, Weber Ae and Ivers-Tiffée E 2013 A novel method for measuring the effective conductivity and the contact resistance of porous electrodes for lithium-ion batteries *Electrochem. Commun.* **34** 130–3

[155] Thorat I V, Joshi T, Zaghib K, Harb J N and Wheeler D R 2011 Understanding rate-limiting mechanisms in $LiFePO_4$ cathodes for Li-ion batteries *J. Electrochem. Soc.* **158** A1185

[156] Bauer W, Nötzel D, Wenzel V and Nirschl H 2015 Influence of dry mixing and distribution of conductive additives in cathodes for lithium ion batteries *J. Power Sources* **288** 359–67

[157] Wei Q, Suga H, Ikeda I, Mukaida M, Kirihara K, Naitoh Y and Ishida T 2016 An accurate method to determine the through-plane electrical conductivity and to study transport properties in film samples *Org. Electron.* **38** 264–70

[158] Weppner W and Huggins R A 1977 Determination of the kinetic parameters of mixed-conducting electrodes and application to the system Li_3Sb *J. Electrochem. Soc.* **124** 1569

[159] Wen C J and Huggins R A 1980 Thermodynamic and mass transport properties of "LiIn" *Mater. Res. Bull.* **15** 1225–34

[160] Bard A J and Faulkner L R 2001 *Electrochemical Methods: Fundamentals and Applications* New Jersey

[161] Nickol A, Schied T, Heubner C, Schneider M, Michaelis A, Bobeth M and Cuniberti G 2020 GITT analysis of lithium insertion cathodes for determining the lithium diffusion coefficient at low temperature: challenges and pitfalls *J. Electrochem. Soc.* **167** 090546

[162] Heubner C, Schneider M and Michaelis A 2016 SoC dependent kinetic parameters of insertion electrodes from staircase—GITT *J. Electroanal. Chem.* **767** 18–23

[163] Chien Y-C, Liu H, Menon A S, Brant W R, Brandell D and Lacey M J 2021 A fast alternative to the galvanostatic intermittent titration technique (https://doi.org/10.33774/chemrxiv-2021-09srz)

[164] Geng Z, Chien Y-C,Lacey M J, Thiringer T and Brandell D 2021 Validity of solid-state Li+ diffusion coefficient estimation by electrochemical approaches for lithium-ion batteries (arXiv:2110.07724 [physics.chem-ph])

[165] Shen Z, Cao L, Rahn C D and Wang C-Y 2013 Least squares galvanostatic intermittent titration technique (LS-GITT) for accurate solid phase diffusivity measurement *J. Electrochem. Soc.* **160** A1842–6

[166] Horner J S, Whang G, Ashby D S, Kolesnichenko I V, Lambert T N, Dunn B S, Talin A A and Roberts S A 2021 Electrochemical modeling of GITT measurements for improved solid-state diffusion coefficient evaluation *ACS Appl. Energy Mater.* **4** 11460–9

[167] Compton R G, Kätelhön E, Ward K R and Laborda E 2014 *Understanding Voltammetry: Simulation of Electrode Processes* (Singapore: World Scientific)

[168] Levi M D, Salitra G, Markovsky B, Teller H, Aurbach D, Heider U and Heider L 1999 Solid-state electrochemical kinetics of Li-ion intercalation into $Li_{1-x}CoO_2$: simultaneous application of electroanalytical techniques SSCV, PITT and EIS *J. Electrochem. Soc.* **146** 1279

[169] Vassiliev S Y, Levin E E and Nikitina V A 2016 Kinetic analysis of lithium intercalating systems: cyclic voltammetry *Electrochim. Acta* **190** 1087–99

[170] Benedek P *et al* 2020 Quantifying diffusion through interfaces of lithium-ion battery active materials *ACS Appl. Mater. Interfaces* **12** 16243–9

[171] Kim T, Choi W, Shin H-C, Choi J-Y, Kim J M, Park M-S and Yoon W-S 2020 Applications of voltammetry in lithium ion battery research *J. Electrochem. Sci. Technol.* **11** 14–25

[172] Pender J P *et al* 2020 Electrode degradation in lithium-ion batteries *ACS Nano* **14** 1243–95

[173] Yu D Y W, Fietzek C, Weydanz W, Donoue K, Inoue T, Kurokawa H and Fujitani S 2007 Study of LiFePO$_4$ by cyclic voltammetry *J. Electrochem. Soc.* **154** A253

[174] Takahashi M 2002 Reaction behavior of LiFePO$_4$ as a cathode material for rechargeable lithium batteries *Solid State Ion.* **148** 283–9

[175] Weppner W and Huggins R A 1978 Electrochemical methods for determining kinetic properties of solids *Annu. Rev. Mater. Sci.* **8** 269–311

[176] John Wen C, Boukamp B A, Huggins R A and Weppner W 1979 Thermodynamic and mass transport properties of "LiAl" *J. Electrochem. Soc.* **126** 2258

[177] Xie J, Imanishi N, Zhang T, Hirano A, Takeda Y and Yamamoto O 2009 Li-ion diffusion kinetics in LiFePO$_4$ thin film prepared by radio frequency magnetron sputtering *Electrochim. Acta* **54** 4631–7

[178] Malifarge S, Delobel B and Delacourt C 2017 Guidelines for the analysis of data from the potentiostatic intermittent titration technique on battery electrodes *J. Electrochem. Soc.* **164** A3925–32

[179] Li J, Xiao X, Yang F, Verbrugge M W and Cheng Y-T 2012 Potentiostatic intermittent titration technique for electrodes governed by diffusion and interfacial reaction *J. Phys. Chem. C* **116** 1472–8

[180] Han B C, Van der Ven A, Morgan D and Ceder G 2004 Electrochemical modeling of intercalation processes with phase field models *Electrochim. Acta* **49** 4691–9

[181] Levi M D and Aurbach D 2012 Potentiostatic and galvanostatic intermittent titration techniques *Charact. Mater.* 913–32

[182] Swiderska-Mocek A and Lewandowski A 2017 Kinetics of Li-ion transfer reaction at LiMn$_2$O$_4$, LiCoO$_2$ and LiFePO$_4$ cathodes *J. Solid State Electrochem.* **21** 1365–72

[183] Chang Y-C, Jong J-H and Fey G T-K 2000 Kinetic characterization of the electrochemical intercalation of lithium ions into graphite electrodes *J. Electrochem. Soc.* **147** 2033

[184] Verbrugge M W and Koch B J 1999 Electrochemistry of intercalation materials charge-transfer reaction and intercalate diffusion in porous electrodes *J. Electrochem. Soc.* **146** 833–9

[185] Zhuang Q, Xu J, Fan X, Dong Q, Jiang Y, Huang L and Sun S 2007 An electrochemical impedance spectroscopic study of the electronic and ionic transport properties of LiCoO$_2$ cathode *Chin. Sci. Bull.* **52** 1187–95

[186] Pistoia G, Antonini A, Rosati R and Zane D 1996 Storage characteristics of cathodes for Li-ion batteries *Electrochim. Acta* **41** 2683–9

[187] Swamy T and Chiang Y-M 2015 Electrochemical charge transfer reaction kinetics at the silicon-liquid electrolyte interface *J. Electrochem. Soc.* **162** A7129–34

[188] Amin R and Belharouak I 2017 Part-II: exchange current density and ionic diffusivity studies on the ordered and disordered spinel LiNi$_{0.5}$Mn$_{1.5}$O$_4$ cathode *J. Power Sources* **348** 318–25

[189] Keefe A S, Buteau S, Hill I G and Dahn J R 2019 Temperature dependent EIS studies separating charge transfer impedance from contact impedance in lithium-ion symmetric cells *J. Electrochem. Soc.* **166** A3272–9

[190] Sikha G and White R E 2007 Analytical expression for the impedance response of an insertion electrode cell *J. Electrochem. Soc.* **154** A43

[191] Song J and Bazant M Z 2013 Effects of nanoparticle geometry and size distribution on diffusion impedance of battery electrodes *J. Electrochem. Soc.* **160** A15–A24

[192] Deng C and Lu. W 2020 Consistent diffusivity measurement between galvanostatic intermittent titration technique and electrochemical impedance spectroscopy *J. Power Sources* **473** 228613

[193] Ivanishchev A V, Ushakov A V, Ivanishcheva I A, Churikov A V, Mironov A V, Fedotov S S, Khasanova N R and Antipov E V 2017 Structural and electrochemical study of fast Li diffusion in Li$_3$V$_2$(PO$_4$)$_3$-based electrode material *Electrochim. Acta* **230** 479–91

[194] Barai A, Uddin K, Dubarry M, Somerville L, McGordon A, Jennings P and Bloom I 2019 A comparison of methodologies for the non-invasive characterisation of commercial Li-ion cells *Prog. Energy Combust. Sci.* **72** 1–31

[195] Newman J 2012 *Electrochemical Systems* (New York: Wiley)

[196] Newman J and Chapman T W 1973 Restricted diffusion in binary solutions *AIChE J.* **19** 343–8

[197] Bizeray A M, Howey D A and Monroe C W 2016 Resolving a discrepancy in diffusion potentials, with a case study for Li-ion batteries *J. Electrochem. Soc.* **163** E223–9

[198] Richardson G W, Foster J M, Ranom R, Please C P and Ramos A M 2020 Charge transport modelling of lithium ion batteries (arXiv:2002.00806 [physics.chem-ph])

[199] Thompson L M, Stone W, Eldesoky A, Smith N K, McFarlane C R M, Kim J S, Johnson M B, Petibon R and Dahn J R 2018 Quantifying changes to the electrolyte and negative electrode in aged NMC532/graphite lithium-ion cells *J. Electrochem. Soc.* **165** A2732–40

[200] Ding M S, Xu K, Zhang S S, Amine K, Henriksen G L and Jow T R 2001 Change of conductivity with salt content, solvent composition and temperature for electrolytes of LiPF$_6$ in ethylene carbonate-ethyl methyl carbonate *J. Electrochem. Soc.* **148** A1196

[201] Nyman A, Behm Mårten and Lindbergh Goran 2008 Electrochemical characterisation and modelling of the mass transport phenomena in LiPF$_6$–EC–EMC electrolyte *Electrochim. Acta* **53** 6356–65

[202] Debye P and Hückel E 1923 Zur theorie der elektrolyte II *Phys. Z.* **24** 305

[203] Onsager L and Fuoss R M 1932 Irreversible processes in electrolytes. diffusion, conductance and viscous flow in arbitrary mixtures of strong electrolytes *J. Phys. Chem.* **36** 2689–778

[204] Hou T and Monroe C W 2020 Composition-dependent thermodynamic and mass-transport characterization of lithium hexafluorophosphate in propylene carbonate *Electrochim. Acta* **332** 135085

[205] Valøen L O and Reimers J N 2005 Transport properties of LiPF$_6$-based Li-ion battery electrolytes *J. Electrochem. Soc.* **152** A882

[206] Landesfeind J and Gasteiger H A 2019 Temperature and concentration dependence of the ionic transport properties of lithium-ion battery electrolytes *J. Electrochem. Soc.* **166** A3079–97

[207] Petrowsky M and Frech R 2009 Temperature dependence of ion transport: the compensated Arrhenius equation *J. Phys. Chem. B* **113** 5996–6000

[208] Xu. K 2004 Nonaqueous liquid electrolytes for lithium-based rechargeable batteries *Chem. Rev.* **104** 4303–418

[209] Wang A A, Hou T, Karanjavala M and Monroe C W 2020 Shifting-reference concentration cells to refine composition-dependent transport characterization of binary lithium-ion electrolytes *Electrochim. Acta* **358** 136688

[210] Prada E, Di Domenico D, Creff Y, Bernard J, Sauvant-Moynot V and Huet F 2012 Simplified electrochemical and thermal model of LiFePO$_4$-graphite Li-ion batteries for fast charge applications *J. Electrochem. Soc.* **159** A1508–19

[211] Kim S U and Srinivasan V 2016 A method for estimating transport properties of concentrated electrolytes from self-diffusion data *J. Electrochem. Soc.* **163** A2977–80

[212] Fong K D, Self J, Diederichsen K M, Wood B M, McCloskey B D and Persson K A 2019 Ion transport and the true transference number in nonaqueous polyelectrolyte solutions for lithium ion batteries *ACS Cent. Sci.* **5** 1250–60

[213] Liu J and Monroe C W 2014 Solute-volume effects in electrolyte transport *Electrochim. Acta* **135** 447–60

[214] Liu J and Monroe C W 2015 On the characterization of battery electrolytes with polarization cells *Electrochim. Acta* **167** 357–63

[215] Diederichsen K M, McShane E J and McCloskey B D 2017 Promising routes to a high Li$^+$ transference number electrolyte for lithium ion batteries *ACS Energy Lett.* **2** 2563–75

[216] Zugmann S, Fleischmann M, Amereller M, Gschwind R M, Wiemhöfer H D and Gores H J 2011 Measurement of transference numbers for lithium ion electrolytes via four different methods, a comparative study *Electrochim. Acta* **56** 3926–33

[217] Villaluenga I, Pesko D M, Timachova K, Feng Z, Newman J, Srinivasan V and Balsara N P 2018 Negative Stefan-Maxwell diffusion coefficients and complete electrochemical transport characterization of homopolymer and block copolymer electrolytes *J. Electrochem. Soc.* **165** A2766–73

[218] Richardson G, Foster J M, Sethurajan A K, Krachkovskiy S A, Halalay I C, Goward G R and Protas B 2018 The effect of ionic aggregates on the transport of charged species in lithium electrolyte solutions *J. Electrochem. Soc.* **165** H561–7

[219] Sethurajan A K, Foster J M, Richardson G, Krachkovskiy S A, David Bazak J, Goward G R and Protas B 2019 Incorporating dendrite growth into continuum models of electrolytes: insights from NMR measurements and inverse modeling *J. Electrochem. Soc.* **166** A1591–602

[220] Robinson R A and Stokes R H 2012 *Electrolyte Solutions* 2nd edn (Mineola: Dover Publications, Incorporated)

[221] Stewart S G and Newman J 2008 The use of UV/vis absorption to measure diffusion coefficients in LiPF$_6$ electrolytic solutions *J. Electrochem. Soc.* **155** F13

[222] Chandrasekaran R and Fuller T F 2011 Analysis of the lithium-ion insertion silicon composite electrode/separator/lithium foil cell *J. Electrochem. Soc.* **158** A859

[223] David Bazak J, Allen J P, Krachkovskiy S A and Goward G R 2020 Mapping of lithium-ion battery electrolyte transport properties and limiting currents with in situ MRI *J. Electrochem. Soc.* **167** 140518

[224] Fawdon J, Ihli J, La Mantia F L and Pasta M 2021 Characterising lithium-ion electrolytes via operando Raman microspectroscopy *Nat. Commun.* **12** 4053

[225] Lundgren H, Behm M and Lindbergh G 2015 Electrochemical characterization and temperature dependency of mass-transport properties of LiPF$_6$ in EC:DEC *J. Electrochem. Soc.* **162** A413–20

[226] Logan E R, Tonita E M, Gering K L, Li J, Ma X, Beaulieu L Y and Dahn J R 2018 A study of the physical properties of Li-ion battery electrolytes containing esters *J. Electrochem. Soc.* **165** A21–A30

[227] Xiong D J, Bauer M, Ellis L D, Hynes T, Hyatt S, Hall D S and Dahn J R 2018 Some physical properties of ethylene carbonate-free electrolytes *J. Electrochem. Soc.* **165** A126–31

[228] Wohde F, Balabajew M and Roling B 2016 Li$^+$ transference numbers in liquid electrolytes obtained by very-low-frequency impedance spectroscopy at variable electrode distances *J. Electrochem. Soc.* **163** A714–21

[229] Shah D B, Olson K R, Karny A, Mecham S J, DeSimone J M and Balsara N P 2017 Effect of anion size on conductivity and transference number of perfluoroether electrolytes with lithium salts *J. Electrochem. Soc.* **164** A3511–7

[230] Pollard R and Comte T 1989 Determination of transport properties for solid electrolytes from the impedance of thin layer cells *J. Electrochem. Soc.* **136** 3734–48

[231] Klett M, Giesecke M, Nyman A, Hallberg F, Lindström R W, Lindbergh G and Furó Ian 2012 Quantifying mass transport during polarization in a Li ion battery electrolyte by in Situ$_7$ Li NMR imaging *J. Am. Chem. Soc.* **134** 14654–7

[232] Bergstrom H K, Fong K D and McCloskey B D 2021 Interfacial effects on transport coefficient measurements in Li-ion battery electrolytes *J. Electrochem. Soc.* **168** 060543

[233] Ehrl A, Landesfeind J, Wall W A and Gasteiger H A 2017 Determination of transport parameters in liquid binary electrolytes: Part II. transference number *J. Electrochem. Soc.* **164** A2716–31

[234] Farkhondeh M, Pritzker M, Delacourt C, Liu S S-W and Fowler M 2017 Method of the four-electrode electrochemical cell for the characterization of concentrated binary electrolytes: theory and application *J. Phys. Chem.* C **121** 4112–29

[235] Harned H S and French D M 1945 A conductance method for the determination of the diffusion coefficients of electrolytes *Ann. New York Acad. Sci.* **46** 267–84

[236] Thompson S D and Newman J 1989 Differential diffusion coefficients of sodium polysulfide melts *J. Electrochem. Soc.* **136** 3362–9

[237] Lundgren H, Scheers J, Behm Mårten and Lindbergh G 2015 Characterization of the mass-transport phenomena in a superconcentrated LiTFSI:Acetonitrile electrolyte *J. Electrochem. Soc.* **162** A1334–40

[238] Bruce P G and Vincent C A 1987 Steady state current flow in solid binary electrolyte cells *J. Electroanal. Chem. Interfacial Electrochem.* **225** 1–17

[239] Galluzzo M D, Loo W S, Schaible E, Zhu C and Balsara N P 2020 Dynamic structure and phase behavior of a block copolymer electrolyte under dc polarization *ACS Appl. Mater. Interfaces* **12** 57421–30

[240] Balsara N P and Newman J 2015 Relationship between steady-state current in symmetric cells and transference number of electrolytes comprising univalent and multivalent ions *J. Electrochem. Soc.* **162** A2720–2

[241] Zyskin M 2021 Unified transform solution of a convection-diffusion equation, and polarisation cell experiment

[242] Wang A A, Gunnarsdóttir A B, Fawdon J, Pasta M, Grey C P and Monroe C W 2021 Potentiometric MRI of a Superconcentrated lithium electrolyte: testing the irreversible thermodynamics approach *ACS Energy Lett.* **6** 3086–95

[243] Sethurajan A K, Krachkovskiy S A, Halalay I C, Goward G R and Protas B 2015 Accurate characterization of ion transport properties in binary symmetric electrolytes using in situ NMR imaging and inverse modeling *J. Phys. Chem.* B **119** 12238–48

[244] Krachkovskiy S A, Bazak J D, Fraser S, Halalay I C and Goward G R 2017 Determination of mass transfer parameters and ionic association of LiPF$_6$: organic carbonates solutions *J. Electrochem. Soc.* **164** A912–6

[245] Feng Z, Higa K, Han K S and Srinivasan V 2017 Evaluating transport properties and ionic dissociation of LiPF$_6$ in concentrated electrolyte *J. Electrochem. Soc.* **164** A2434–40

[246] Gouverneur M, Kopp J, van Wüllen L and Schönhoff M 2015 Direct determination of ionic transference numbers in ionic liquids by electrophoretic NMR *Phys. Chem. Chem. Phys.* **17** 30680–6

[247] Timachova K, Newman J and Balsara N P 2019 Theoretical interpretation of ion velocities in concentrated electrolytes measured by electrophoretic NMR *J. Electrochem. Soc.* **166** A264–7

[248] Ward L *et al* 2021 Principles of the battery data genome (arXiv:2109.07278 [physics.soc-ph])

[249] De Angelis V, Preger Y and Chalamala B R 2021 Battery lifecycle framework: a flexible repository and visualization tool for battery data from materials development to field implementation *ECS Arxiv* (https://doi.org/10.1149/osf.io/h7c24)

[250] dos Reis Gçalo, Strange C, Yadav M and Li S 2021 Lithium-ion battery data and where to find it *Energy AI* **5** 100081

[251] Jain A *et al* 2013 Commentary: The materials project: a materials genome approach to accelerating materials innovation *APL Mater.* **1** 011002

[252] Huang S and Cole J M 2020 A database of battery materials auto-generated using ChemDataExtractor *Sci. Data* **7** 260

[253] El-Bousiydy H, Lombardo T, Primo E N, Duquesnoy M, Morcrette M, Johansson P, Simon P, Grimaud A and Franco A A 2021 What can text mining tell us about lithium-ion battery researchers' habits? *Batteries Supercaps* **4** 758–66

[254] Mistry A *et al* 2021 A minimal information set to enable verifiable theoretical battery research *ACS Energy Lett* **6** 3831–5